

THE
MODELLING
OF
ISOLATED DENSE
C O R E S

IN THE W51

INFRA RED DARK CLOUD

MASTER THESIS

CHRISTIAAN WESSEL ORMEL

UNDER THE SUPERVISION OF

FRANK HELMICH RUSSELL F. SHIPMAN VOLKER OSSENKOPF

Contents

Preface	v
1. Introduction	1
2. Continuum modelling of Infrared Dark Cloud Cores	9
3. HCO ⁺ line modelling of Infrared Dark Cloud Cores	23
4. Concluding Remarks	37
List of Acronyms	39
Acknowledgments	41

Preface

This *Master Thesis* consists of four parts:

- Introduction
- *Continuum modelling of IRDC Cores* (Paper I)
- *HCO⁺ line modelling of three IRDC Cores* (Paper II)
- Concluding Remarks

The core of this thesis consist of the papers, which deal with the actual research of this project. The first paper is intended for publication. It contains the results of the dust modelling of three cores within the W51-IRDC region. In the second paper the modelling is extended to molecular lines, for which HCO⁺ is treated as a pilot. Although this part is not yet intended as a formal paper, it is simply referred to as ‘Paper II’ throughout the thesis.

The introduction starts with a quick review of the context, i.e. the still unfinished Star Formation debate. Also discussed here is the discovery of Infrared Dark Clouds, focusing in particular on the IRDC central to this project. Finally, this thesis finishes with some concluding remarks and sincere acknowledgments.

I. Introduction

1.1 The Star-Formation issue: A short review

Stars

Although 20th century astronomy expanded its focus beyond the stellar zoo of the Milky Way galaxy, the study of stars continued to yield fruitful results. Stellar Evolution models (e.g. Iben, 1967) can explain all stellar stages – ranging from the nativity of the Hayashi Track, the steady state ‘Main-Sequence’, the Red-, Horizontal- and Asymptotic giant branches to the explosive finality of supernovae. It was found that the primary parameter determining the stellar evolution is the *mass* of the newly-born star.¹ It determines its luminosity and lifetime (high mass stars ‘burn’ faster and live shorter), the stage nuclear fusion in the stellar core will advance to and it seals the fate of the star itself: whether it will slowly burn-out as a White Dwarf (low mass stars) or go supernova (high mass stars) and produce the more ‘extreme’ objects of the universe (pulsars, black holes).

Although relatively obscure regarding numbers, it is the high-mass stars ($M > 8M_{\odot}$) that should deserve special attention. Their effective temperature T_{eff} at which they radiate away their nuclear energy is high enough to produce significant quantities of photons with energies $E > 13.6$ eV, capable of ionizing neutral hydrogen, producing HII regions. Together with their strong stellar winds, high radiation pressure and the fact that they end violently in Supernovae, high mass stars decisively influence their immediate surroundings and – on a larger scale – the Galaxy’s interstellar medium (ISM).² Finally, there is a more practical argument that makes high-mass stars special: Because of their large luminosities they are the easiest to observe.

The IMF

This introduction emphasizes the importance of understanding *how* high-mass stars or stars in general are *formed*. Critical in answering this question is to get an understanding of the *Initial Mass Function* (IMF): The distribution of masses at which stars are

¹It is not claimed properties such as metallicity are unimportant. Indeed these properties are in fact key parameters for understanding evolutionary effects.

²All acronyms are listed separately on page 39.

formed. Various distributions have been proposed, but none has been so commonly used as the one by that of Salpeter: (Salpeter, 1955)

$$dN = N(M) dM \propto M^{-\gamma} dM \quad \gamma \approx 2.35 \quad (1.1)$$

is the number of stars within the mass interval $M, M + dM$. For a Salpeter distribution $N(M)$ obeys a power-law with negative exponent $-\gamma$. Hence low-mass stars are much more numerous and also dominate by total mass.³ However, since negative exponents cause power-laws to diverge toward zero, the IMF has to have a lower limit. Indeed for low masses it flattens to $\gamma \approx 1.3$ at $M = 0.5 M_{\odot}$ and even further to $\gamma \approx 0.3$ at $M = 0.08 M_{\odot}$ (Kroupa, 2001).

While from an observational point of view the IMF has been established at $\gamma \approx 2.35$ (at least for $M \gtrsim 2.8 M_{\odot}$; Massey (1998); Massey & Hunter (1998)),⁴ there is still ongoing debate about the mechanisms causing the particular IMF. These mechanisms are in fact the mechanisms of star formation (SF) and – since in these stages stars do not appear as twinkling objects in the sky, making observing them a lot more difficult – it is the SF-problem that continuous to puzzle astronomers. For example, it is found that the IMF is rather insensitive to environment (e.g. density and metallicity of the progenitor cloud), while this is not expected, since e.g. metallicity determines the cooling and thus the fragmentation behaviour. Perhaps magnetic fields play a pivotal role in obtaining the $\gamma \approx 2.35$ value as is suggested by Shu et al. (2004).

Although the Salpeter law, while having reached its 50th anniversary, has been well established to hold globally, on local scales the IMF can be very different. Herbig (1962) noticed qualitative differences between the Taurus region of SF, in which no stars more massive than $\sim 2 M_{\odot}$ were found, and that of Orion, which contained many high mass young stellar objects (YSOs) together with lower mass counterparts. This *bimodal* SF was first speculated to be an evolutionary effect, but current observations strongly favour a real *spatial* distinction. While low-mass SF-regions are linked to cold molecular clouds, high mass SF seems to be associated with giant molecular clouds (GMCs) containing warm cores with temperatures in excess of 20 K. However, high-mass SF is very rare and subsequently much harder to observe, which holds especially for its very earliest stages.

Cores

Gravity must naturally be the key to every SF-theory. An useful concept is the Jeans mass: the maximum mass to which thermal pressure through the virial theorem (potential + 2 * kinetic energy = 0) can resist gravity:

$$M_J = \left(\frac{3}{4\pi}\right)^{1/2} \left(\frac{5k}{\mu m_H G}\right)^{3/2} \rho^{-1/2} T^{3/2} \approx 10 M_{\odot} \left(\frac{T}{15 \text{ K}}\right)^{3/2} \left(\frac{n}{10^4 \text{ cm}^3}\right)^{-1/2} \quad (1.2)$$

³To determine $N(M)$ is in fact not trivial. Since stars cannot be weighed, its place in the HR-diagram (luminosity, effective temperature) is converted into a mass, using isochrones of stellar evolution models.

⁴Note that these values for γ are unaccounted for binary stars. Since massive stars probably have many companions, the binary-corrected values of γ is higher.

(for an iso-thermal, iso-dense cloud with $\mu = 2.26$, the mean molecular weight; k , G and m_{H} being Boltzmann’s constant, Newton’s Gravitational constant and the hydrogen mass respectively). As densities rise and temperatures drop this lowers M_{J} and the cloud will collapse. But during collapse, the contraction releases thermal energy, preventing further fragmentation. Bonnor and Ebert (Bonnor (1956), Ebert (1957)) included outside radiation pressure and found that central over boundary densities of $\rho_c/\rho_b > 13.98$ are unstable.⁵ Shu (1977) examined hydrodynamically unstable cores and, starting with a $1/r^2$ density distribution of isothermal spheres, found a similarity solution corresponding to an inside-out collapse scenario in which an expansion wave propagating outwardly separates an inner $\rho \propto r^{-3/2}$ density distribution associated to free-fall from an outer $\rho \propto r^{-2}$ regime.

Nevertheless the number of observed dense cores/clouds is such, that not all of them can be supercritical. They would otherwise collapse on a free-fall time scale,

$$t_{\text{ff}} = \sqrt{\frac{3\pi}{32G\rho}} \approx 0.34 \text{ Myr} \left(\frac{n}{10^4 \text{ cm}^{-3}} \right)^{-1/2}, \quad (1.3)$$

but then the SF in the Galaxy would be far higher than the typically quoted $3 - 5 M_{\odot} \text{ yr}^{-1}$. So the SF-*efficiency* is small and the (far more massive) surrounding clouds especially require additional, non-thermal support. Various means of support have been proposed: rotation, turbulence and magnetic fields. Rotation seems not to play a dominant role on scales of the cloud size, but ultimately – in order to form disks out of which planetary systems might evolve – spherical symmetry must be broken. Magnetic fields have the advantage that they are not easily dissipated (like turbulence) and therefore give a natural explanation of why cores do *not* ‘immediately’ turn into stars.

Radiative transfer

Isothermality is an assumption which seems hard to justify, since dense cores effectively shield the interstellar radiation field (ISRF). This ISRF consist of four components: (Mathis et al., 1983) The UV-radiation from young OB-stars, the NIR part from red giants stars, the MIR/FIR radiation from the dusty galactic plane and finally the 2.7 K component from the Cosmic Microwave Background (CMB). So, in the outer layers of the cores temperature gradients must be present, while in the inner densest regions the temperature stabilizes to values of 7 – 10 K due to heating by cosmic rays. Considering these heating mechanisms, an important remark is that – although the dynamics is dominated by molecular hydrogen, which constitutes most of the mass – it is the *dust* that dominates the radiation transport and a dust to gas ratio (typically 100 – 200 in mass) has to be assumed when translating these into another. This dust, which consists of a mixture of silicate and graphite grains, effectively absorbs the high energy photons and reradiates at the equilibrium temperature ($\sim 10 - 20$ K), i.e. in the

⁵Lombardi & Bertin (2001) have shown this relation is in fact geometry-dependent, but that a similar relation, $\bar{\rho} > 2.46\rho_b$, in which $\bar{\rho}$ is the mean density, is independent of geometry.

sub-mm regime of the electromagnetic spectrum. Leung (1975) set up such a radiative transfer model and found, depending on the specific grain types, Temperatures dropping to (3 – 8) K for spherical clouds.⁶ The choice for the specific dust model – which determines the opacities, $\kappa(\nu)$, and subsequently the emission rates, $j(\nu) = \kappa(\nu)B(\nu, T)$, where $B(\nu, T)$ is Planck’s function – is therefore critical. Ossenkopf & Henning (1994) have computed opacities from a MRN distribution of grains,⁷ which took into account ice-mantles and grain-coagulation effects.

In this work we will confront the stability of cores from an observational point of view and use radiative transfer models as the link to the physical and evolutionary state of the cores. Continuum radiation models of sub-mm dust observations for example can constrain (a range of) density distributions and are therefore critical in testing theoretical predictions. The `csdust3` code of Egan et al. (1988) – used in this project and explained more thoroughly in Appendix A of Paper I – is such a code. The connection between the model results and the observations is usually expressed in the χ^2 goodness-of-fit parameters. And the aim is twofold: *i* to find a fit as good as possible by minimizing χ^2 and *ii* to test how the quality of the fit is sensitive to variation of the fit parameters, thereby setting constraints on these parameters.

Molecules

Apart from the physical point of view, the evolution of molecular clouds/cores is also expressed in their chemistry. While (ionized) atoms are observed in great variety throughout the (hot) ISM, the more complex structures (i.e. molecules) can only be formed within molecular cores, which are shielded from dissociative photons. Moreover, in these coldest parts of the ISM species become frozen out and the chemistry is dominated by reactions which take place on the surfaces of grains. In this way the CO-hydrogenation (taking place in the grain’s ice layer) leads to H₂CO (formaldehyde) and in the next steps to CH₃OH (methanol). Longer, more complex structures like ethers and esters have been observed in hot cores, where the ice-mantles have evaporated. The total number of detected molecules exceeds 100 and since all species are inter-related, chemical modelling might seem complex. However, if the reaction rates and the initial physical and chemical conditions are accurately known (which is not always the case), the abundance of a particular species can easily be calculated. The difficult part comes from the fact that the chemical composition determines the strength of the magnetic field (via its electron fraction) and the gas cooling rate and is in its turn intrinsically related to the physical conditions.

The presence of (complex) molecules is also important from an observational point of view, since the strength of molecular lines is an important diagnostic of the region under consideration. This depends, apart from the molecular abundance, on the state to which the molecule is excited – i.e. to which extent the upper level is populated –,

⁶This code, like the code used in this project, does not account for cosmic ray heating.

⁷MRN = Mathis, Rumpl and Nordsieck, Mathis et al. (1977).

which is a sensitive function of the local physical conditions. Especially the combination of multiple transitions as measured in different rotational levels, can constrain observations (Jansen, PhD-thesis), though the interpretation in a situation of density and temperature gradients is not straightforward. High density environments of e.g. molecular cores are best probed by molecules with a high critical density. (Defined to be the ratio of the radiative over the collisional rate coefficients,

$$n_{\text{crit}} = \frac{A_{ul}}{\sum_{i \neq u} K_{ui}}. \quad (1.4)$$

Moreover, molecular lines are sensitive to the *dynamics* of the region, i.e. to the velocity structure: Is the region under consideration dominated by turbulence and/or are systematic (infall, rotation, outflows) motions occurring? Also, the intrinsic nature of cores is often found (Hogerheijde et al., 1995) to be clumpy, affecting the emergent line profile. Altogether, in order to mimic these manifestations, observations require the support of detailed line-radiative transfer models indeed.

1.2 Infra-Red Dark Clouds

Infra-Red Dark Clouds (IRDCs) are a relatively new phenomenon in Astronomy, detected only in the later nineties of the last century by Perault et al. (1996) using the Infrared Space Observatory Camera (ISOCAM) and independently by Egan et al. (1998) with the Midcourse Space Experiment (MSX) satellite. IRDCs stand out as silhouettes against the Galaxy's bright Mid Infrared (MIR) background ($8 - 25 \mu\text{m}$), caused by hot dust. To absorb at these wavelength already indicates the presence of large column densities of material. It is the dust that absorbs the MIR-photons, but it also reradiates with an intensity (in the optically thin case) of

$$I_\nu = B_\nu(T_{\text{dust}}) Q_{\text{abs}}(\nu) \pi a^2 N_{\text{dust}}. \quad (1.5)$$

In which $B(\nu, T)$ is the Planck function, N_{dust} the dust column density and $Q_{\text{abs}} \pi a^2$ the effective absorption cross-section of (a distribution of) grains. Therefore, the combination of high column densities and the absence of mid to far infrared emission sets upper limits on the temperature. Carey et al. (1998) following such an analysis, together with H_2CO observations derived temperatures less than 20 K. Most IRDC are detected toward the centre of the Galaxy; toward the 4 kpc galactic ring and toward spiral arms (Egan et al., 1999). However, part of this might well be a selection effect; the bright background alleviates detections, and the possible detection of an IRDC in the outer galaxy (Frieswijk, priv. comm.) could mean IRDCs to be very numerous indeed. In summary IRDC, which are observed in wide geometrical variety –ranging from simple blobs to large, filamentary structures–, are dense, cold, distant and massive.

However, not all IRDC can be characterised as such. Occasionally IRDCs show to harbour spots of IR and sub-mm emission. For example, IRAS point sources have been detected and Carey et al. (2000) show bright, compact sources detected at sub-mm

OBSERVATIONS OF THE W51-IRDC USED IN THIS THESIS

telescope/satellite	wavelength/molecule	main beam	map/pointing
MSX	8.3 μm	18''	map
IRAS ^a	100 μm	220''	
JCMT (SCUBA)	450 μm	7.5''	map
	850 μm	15''	map
JCMT (lines)	HCO ⁺ ... 3 \rightarrow 2	20''	map
	... 4 \rightarrow 3	14''	map
KOSMA	HCO ⁺ ... 3 \rightarrow 2	130''	pnt.: P1, EP
	... 4 \rightarrow 3	82''	pnt.: P1, EP

^a The W51-IRDC was not detected by the IRAS satellite. This non-detection is, however, used to constrain the continuum modelling.

wavelengths, sometimes accompanied by a recognizable feature at 8.3 μm . Since these cores are all very massive, it is speculated high-mass SF is ongoing. Carey et al. (2000) distinguish between Class 0 protostars and Class I,⁸ based on whether MIR emission is present or not. At least 8.3 μm extinction is a perfect tracer to look for sites of high mass SF in its earliest stages.

In this thesis we concentrate on one specific IRDC: The one directed toward W51. W51 is a very luminous GMC populated with newly born stars. It is located at a distance of about 7.5 kpc and lies along the Sagittarius arm of the Galaxy. Near the rim of this huge complex (it extends for several degrees), MSX has detected in absorption two IRDCs, in front of W51. One is spherical and doesn't show much activity, while the other shows an elongated, S-shaped, structure. From HCO⁺ line observations and the galactic rotation curve (Wouterloot & Brand, 1989) a distance of 2.7 kpc to the S-shaped IRDC is derived. Frieswijk (2002) measured the extinction from 2MASS observations using a star count technique and estimated the mass at around $M = 500 M_{\odot}$ for the whole cloud. Subsequent JCMT observations (see below) have shown the presence of three separate condensations, i.e. cores, where the sub-mm emission is enhanced. However, unlike some of Carey's IRDC, these cores are not notable at 8.3 μm and were also not detected by IRAS. However, they stand out significantly with respect to their environment in the sub-mm and it was the discovery of these cores that triggered this research.

1.3 Goal of this work

The goal of this project can be summed up in one phrase: *To derive the physical conditions of three cores within the W51-IRDC.* To accomplish this goal, a wide range of sub-mm observations is available which are interpreted using detailed radiative transfer models. The focus of this project is primarily on the *current* state of these cores. How the results fit in a general picture of IRDC (core) evolution receives less emphasis, since this requires an extension and cataloguing of multiple IRDCs. This project, in contrary, examines in depth the cores of one particular IRDC. The next step obviously is to extend the modelling to other IRDCs/cores and to interpret the difference in results, which will undoubtedly be there.

Observations are available from the JCMT and KOSMA telescopes and from the MSX satellite. Continuum maps of the W51-IRDC1 cloud have been made with JCMT's Submillimeter Common User Bolometer Array (SCUBA). Measured at 450 and 850 micron, these continuum observations clearly show the presence of the cores: One coinciding with the peak of MSX extinction (hence Extinction Peak), while the other two are even more prominent at these wavelengths (emission peaks, P1 and P2). P2, like EP, follows the main stream of MSX-extinction, but P1 lies somewhat away from it, though it is in no way prominent at $8\ \mu\text{m}$. The sub-mm data is modelled in Paper I, while Paper II deals with the modelling of the HCO^+ line observations from both JCMT and KOSMA telescopes. All of the models are spherical symmetric, an assumption that can be justified since the cores are all small with respect to the S-shaped IRDC. However, this approximation should be kept in mind, since spherical symmetry must ultimately fail (see above). Moreover the resolution of the data is such that e.g. 2d-modelling will not be useful anyway and 1d-sphericity serves as a good starting point.

These models should then result in an understanding of the physical structure of these cores. The continuum model of Paper I should give constraints on the density distribution and the temperature distribution, i.e. on the sizes and masses of the cores and on the radial dependence of density and temperature, $n(r)$ and $T(r)$. The temperature structure is, apart from $n(r)$, influenced by the parameters on the boundaries (i.e. at the outer radius R and the inner cut-off radius r_c): the ISRF at R and the strength of a possible source in its centre. This latter aspect is especially of importance: Do the models *require* an inner heating source in order to match the observations? And (if this is true) how strong is this source: Are there e.g. indications of high mass SF?

Using the temperature and density structure as obtained from Paper I, the line modelling of Paper II, for which HCO^+ observations are used, should give an understanding of the dynamics of the cores. Are e.g. systematic motions (infall or outflow) present and is the velocity distribution turbulent in nature? Moreover, the model used in this part is capable of treating the medium as a two component system, reflecting the pos-

⁸The classes represent the shape of the spectral energy distribution (SED) in the IR. Class I is a 'rising' SED, i.e. $s > 0$ as in $F_\lambda d\lambda \propto \lambda^s$, while for Class II $s < 0$. This defines an evolutionary sequence and Class 0 was introduced in cases the SED is dominated at sub-mm wavelengths.

sibly inhomogeneous mass distribution. To summarize: The line-modelling should support the conclusions of Paper I, reveal whether systematic velocities are present and indicate whether the medium is clumped.

References

- Bonnor, W. B. 1956, MNRAS, 116, 351
- Carey, S. J., Clark, F. O., Egan, M. P., Price, S. D., Shipman, R. F., & Kuchar, T. A. 1998, Ap.J., 508, 721
- Carey, S. J., Feldman, P. A., Redman, R. O., Egan, M. P., MacLeod, J. M., & Price, S. D. 2000, Ap.J., 543, L157
- Ebert, R. 1957, Zeitschrift fur Astrophysics, 42, 263
- Egan, M. P., Carey, S. J., Price, S. D., Shipman, R. F., Feldman, P., & Redman, R. 1999, in ESA SP-427: The Universe as Seen by ISO, 671–+
- Egan, M. P., Leung, C. M., & Spagna, G. F. 1988, Computer Physics Communications, 48, 271
- Egan, M. P., Shipman, R. F., Price, S. D., Carey, S. J., Clark, F. O., & Cohen, M. 1998, Ap.J., 494, L199+
- Frieswijk, W. F. 2002, Master Thesis, 1, 1
- Herbig, G. H. 1962, Advances in Astronomy and Astrophysics, 1, 47
- Hogerheijde, M. R., Jansen, D. J., & van Dishoeck, E. F. 1995, Astron. & Astrophys., 294, 792
- Iben, I. 1967, Ann. Rev. Astron. Astrophys., 5, 571
- Kroupa, P. 2001, MNRAS, 322, 231
- Leung, C. M. 1975, Ap.J., 199, 340
- Lombardi, M. & Bertin, G. 2001, Ap.J., 375, 1091
- Massey, P. 1998, in ASP Conf. Ser. 142: The Stellar Initial Mass Function (38th Herstmonceux Conference), 17–+
- Massey, P. & Hunter, D. A. 1998, Ap.J., 493, 180
- Mathis, J. S., Mezger, P. G., & Panagia, N. 1983, A.&Ap., 128, 212
- Mathis, J. S., Rumpl, W., & Nordsieck, K. H. 1977, Ap.J., 217, 425
- Ossenkopf, V. & Henning, T. 1994, A.&Ap., 291, 943
- Perault, M., Omont, A., Simon, G., Seguin, P., Ojha, D., Blommaert, J., Felli, M., Gilmore, G., Guglielmo, F., Habing, H., Price, S., Robin, A., de Batz, B., Cesarsky, C., Elbaz, D., Epchtein, N., Fouque, P., Guest, S., Levine, D., Pollock, A., Prusti, T., Siebenmorgen, R., Testi, L., & Tiphene, D. 1996, A.&Ap., 315, L165
- Salpeter, E. E. 1955, Ap.J., 121, 161
- Shu, F. H. 1977, Ap.J., 214, 488
- Shu, F. H., Li, Z., & Allen, A. 2004, Ap.J., 601, 930
- Wouterloot, J. G. A. & Brand, J. 1989, A.&Ap., 80, 149

II. Continuum modelling

of IRDC cores

Continuum Modelling of InfraRed Dark Cloud Cores

C.W. Ormel¹, R.F. Shipman^{1,2}, F.P. Helmich^{1,2}, and V. Ossenkopf^{2,3}

¹ Kapteyn Astronomical Institute, PO box 800, 9700 AV Groningen, The Netherlands
e-mail: ormel@astro.rug.nl

² SRON National Institute for Space Research, PO box 800, 9700 AV Groningen, The Netherlands
e-mail: russ@sron.rug.nl
e-mail: f.p.helmich@sron.rug.nl

³ i. Physikalisches Institut, Universität zu Köln, Zùlpicher StraÙe 77, 50937 Köln, Germany
e-mail: ossk@ph1.uni-koeln.de

Abstract. Continuum emission at 450 μm and 850 μm from three distinct cores of an infrared dark cloud toward W51 have been modelled using a self-consistent dust radiative transfer code. Two of these cores show prominent sub-millimeter emission, while the third corresponds to the peak of 8.3 μm extinction as measured by MSX. The model results, expressed in the χ^2 -quality-of-fit parameter, were also constrained by the absence of 100 μm emission from IRAS. Taking these data sets into account, the model was inconclusive about whether the peak of MSX-extinction is associated with an internal heating source or not. The two newly determined emission peaks, though, were found associated with a source and should contain heating equivalent of $\sim 300 L_{\odot}$. The core masses range from 70 – 150 M_{\odot} and their density distribution is similar to more evolved regions of high-mass star formation.

Key words. Molecular Cores – Radiative Transfer Modelling – Dust

1. Introduction

InfraRed Dark Clouds (IRDC) have been observed in recent mid IR surveys of the Galactic Plane (Perault et al., 1996; Egan et al., 1998) as prominent absorption features against the bright mid IR Galactic emission. Due to their lack of 60 μm and 100 μm emission, IRDCs must be cold, i.e. below 30 K. This cold nature is confirmed, by follow up observations of molecular lines and sub-mm continuum observations placing most IRDCs below 15 K (Carey et al., 1998; Teyssier et al., 2002). Furthermore, these line observations provided a radial velocity and hence estimates of the distances. Most IRDCs are at distances greater than 1 kpc and are preferentially located toward spiral arms and the galactic ring (Egan et al., 1999).

Nowadays, thousands of IRDCs have been found throughout the Galactic Plane and counterparts are found at different wavelengths. Carey et al. (2000) identified a number of IRDCs from the Midcourse Space Experiment (MSX) Galactic Plane survey (Price et al., 2001) and observed these IRDCs in 850 μm dust continuum emission. They find a variety of sources or cores associated with the IRDCs. Most of these ‘sources’ are seen in absorption at 8.3 μm , but occasionally in emission. Carey et al. (2000) find masses ranging from 20 M_{\odot} to 1000 M_{\odot} and temperatures that can be characterised as cold (10 K) to warm (40 – 50 K). Redman et al. (2003) continued examining the G79.3+0.3 region and found young stellar ob-

jects to be associated with sub-mm observations at the edge of the IRDC complex.

Because of their sheer size, high column densities and low temperatures, it is suggested that IRDC are the sites of the formation of massive stars. However, unlike low-mass star formation which has a relatively well developed theoretical foundation for all stages, little observational and theoretical information is available on the very early stages of formation of massive stars. The discovery of IRDC might provide a clue on the details of high mass star formation and the difference with its lower-mass counterparts.

Low mass cores have been studied in great detail in the sub-mm, via the spectral energy distribution and modelling of the sub-mm emission. The modelling effort serves to constrain the radial density and temperature structures of the cores and can be compared with theoretical models. These observations generally support theories of star formation in molecular cores (Shirley et al., 2000; Evans et al., 2001; Shirley et al., 2002).

Similar techniques have been applied to high mass protostars in order to probe the physical structure of the envelopes surrounding these sources (van der Tak et al., 2000; Hatchell & van der Tak, 2003; Mueller et al., 2002). The difference between the observations described here and those listed above, is that all but two of the sources listed in the articles above have strong mid to far IR emission. The two sources which show no mid IR emission were only observed at 350 μm and there-

fore not modelled (Mueller et al., 2002). These high mass proto stars, therefore, are objects already relatively well evolved.

There are many questions regarding IRDCs. Do they represent the earliest stages of high mass star formation? If so how do they compare with Bok globules and low mass star formation? If not what is their fate? In order to begin addressing these questions, SCUBA 450 μm and 850 μm data have been obtained toward one IRDC complex seen in the direction of the W51 GMC. This article presents and discusses the physical properties (density and temperature structure and presence of internal heating) of the complex through detailed continuum modelling of the sub-mm dust continuum emission.

This article is organised as follows. Section 2 discusses the observations and data reduction of SCUBA 450 μm and 850 μm . In Sect. 3 the SCUBA and MSX observations are compared to estimate the optical depth. Sect. 4 discusses the azimuthal averaging of the data, a necessary step for the comparison with the spherical-symmetric core-model (Sect. 5). Results are given in Sect. 6 and an overall discussion is presented in Sect. 7.

2. Observations

2.1. MSX Data

The IRDC considered in this article is a complex clearly visible in MSX images (Price et al., 2001) in the direction of the W51 GMC (Fig. 1). The image is in equatorial coordinates and has been centred on the peak extinction which is also at the centre of the S-shaped extinction valley.

2.2. JCMT Line Observations

$\text{HCO}^+ 3 \rightarrow 2$ single pointing line observations and raster scans were obtained at JCMT on 5 December 2001 and 15 September 2003 respectively. From these observations, the radial velocity of the entire complex is found to be 33.5 km s^{-1} which implies a distance of 2.7 kpc (Wouterloot & Brand, 1989).

2.3. JCMT Continuum Observations

JCMT observations¹ of the W51-IRDC cloud were made on October 28, 2002 at 450 μm and 850 μm with the Submillimeter Common User Bolometer Array. The SCUBA observations had good weather conditions ($\tau_{\text{CSO}} \sim 0.06$). To cover the extinction region seen in MSX, a $6'$ by $4'$ area was observed using the scan map mode. Two perpendicular chop angles were used with three chop throws of $30''$, $44''$, $68''$ and the image was reconstructed using the Emerson II technique (Jenness et al., 2000).

The data were flat-fielded, extinction corrected, and calibrated on Uranus using the standard SCUBA reduction software (Jenness & Lightfoot, 1998). During the observations,

¹ The JCMT is operated by the Joint Astronomy Centre in Hilo, Hawaii on behalf of the parent organisations Particle Physics and Astronomy Research Council in the United Kingdom, the National Research Council of Canada and The Netherlands Organisation for Scientific Research.

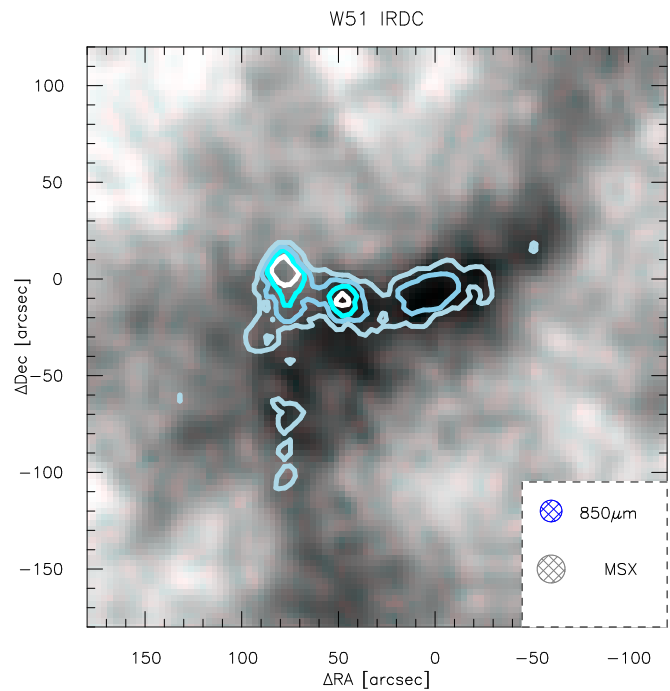


Fig. 1. InfraRed Dark Cloud in the direction of W51 as observed by MSX with SCUBA contours overlaid. The MSX image is stretched from $2.0 \times 10^{-6} \text{ W m}^{-2} \text{ sr}^{-1}$ to $4.5 \times 10^{-6} \text{ W m}^{-2} \text{ sr}^{-1}$. Overlaid are SCUBA emission contours at 4, 6, 8 and 10 times the 850 μm rms level. The zero point of this image is at (RA, DEC) = ($19^{\text{h}}21^{\text{m}}44.7^{\text{s}}$, $13^{\circ}49'34.7''$) and the rms-noise levels are $\sigma_{850} = 0.040 \text{ Jy beam}^{-1}$.

SCUBA was experiencing the transient noise phenomenon associated with contamination caused by superfluid helium films. Over a few days, this noise moved along bolometer arrays, and in this case, moved from the 850 μm array to the 450 μm array. However, over the period of a few hours the noise was stable enough to identify affected bolometers and remove them from further processing. The removal of these bolometers had the main result of increasing the noise in the final image above what one would expect for the assigned observing time. From the final images the noise is estimated at $300 \text{ mJy beam}^{-1}$ at 450 μm and 20 mJy beam^{-1} at 850 μm .

2.3.1. Flux Calibration

Although the calibration should be good to 15% and 25% for the 850 W and 450 W filters respectively (Jenness et al., 2000), the observations were obtained early in the evening when the Flux Conversion Factors (FCF: the conversion from engineering units of Volts to Jy beam^{-1}) can change quite dramatically within the range of times of the observations (Wouterloot, priv. comm.). For the observations presented in this article the FCFs are likely to have declined by 10% and 20% respectively for 850 μm and 450 μm . Unfortunately, two Uranus observations, before and after the observing session were not obtained, thus the impact of the FCF change was not observed.

It is, however, possible to estimate the impact of this calibration change by artificially reducing the 850 μm and 450 μm radial profiles by 10% and 20% respectively and recalculating

BEAM PATTERN		
λ	relative power	FWHM
[μm]	w_i	[$''$]
450.....	0.45	8.0
	0.25	23.5
	0.30	47.0
850.....	0.80	14.6
	0.20	58.8

Table 1. JCMT Beam pattern as observed on Uranus. The total beam is approximated to be a superposition of Gaussians. The 450 μm -beam especially deviates from a single Gaussian, with more than 50% of the power falling into the error beams. The beam profiles are plotted in Fig. 2.

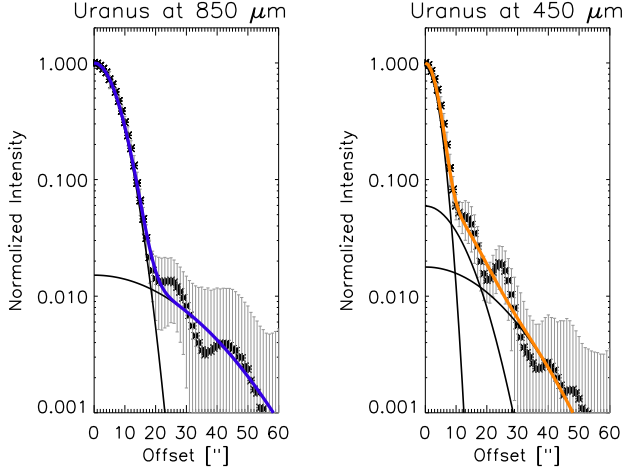


Fig. 2. Beam profiles as measured on Uranus on Oct 28, 2002. The beam profile is represented by a superposition of Gaussians, whose parameters are listed in Table 1. The beam profiles are normalised to their central ($\theta = 0''$) value.

the χ^2 goodness of the fit of the models. (To be addressed in Sect. 5. The main effect is to broaden the χ^2 -topology but not to significantly change the best fitting parameters.) A changing FCF, although increasing the uncertainty in the calibration, does not alter the main findings of this work.

2.3.2. Image Construction

With the Emerson II image reconstruction technique, spatial structures much longer than the 68'' chop throw are not reliably reconstructed (Johnstone et al., 2003). This implies that a local zero correction is necessary in regions of the image smaller than the largest chopper throw of 68''.

2.3.3. SCUBA Beams

Since both SCUBA 450 μm and 850 μm beam patterns are quite complex, azimuthal averages of the Uranus observations were made (Fig. 2). The actual beam pattern differs significantly from a single Gaussian, especially at 450 μm where 55% of the power is not in the main beam. The actual beam pattern,

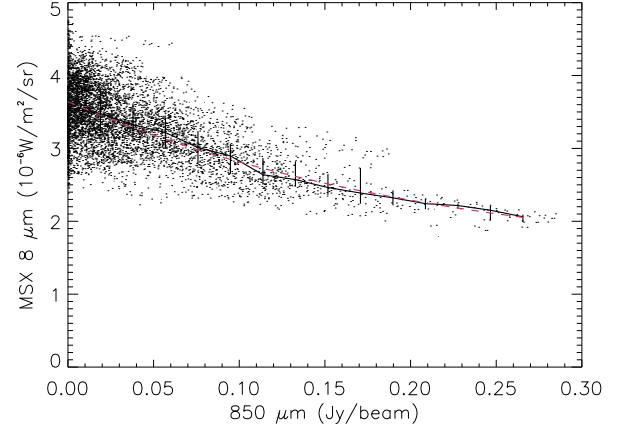


Fig. 3. Anti-correlation between 8.3 μm and 850 μm . The data modelled are shown as the solid line with the model overlaid as a dashed line.

$B(\theta)$, is approximated by a superposition of Gaussians, i.e.

$$B(\theta) = w_1 G_1(\theta, \sigma_1) + w_2 G_2(\theta, \sigma_2) + \dots, \quad (1)$$

where the Gaussians are appropriately normalised to account for the two dimensional nature of the beams and are given by

$$G(\theta, \sigma) = \frac{1}{2\pi\sigma^2} \exp\left[-\frac{\theta^2}{2\sigma^2}\right]. \quad (2)$$

The relative weights w_i of the Gaussians and their FWHMs ($= 2.35 \sigma$) are given in Table 1. Three Gaussians are used to characterise the 450 μm beam and two Gaussians for the 850 μm beam. These approximated beam patterns are used in the modelling described in Sect. 5.

3. Mid-Infrared Extinction

With images of the region in both the mid IR and the sub-mm it is possible to estimate the 8.3 μm opacity within the dark cloud complex. In Sect. 7 this estimate of the mid-IR extinction is compared to the values as given by the continuum modelling. Following Johnstone et al. (2003), the anti-correlation of the 8.3 μm emission with the 850 μm emission is analysed by fitting the mid IR data to the simple model of uniform foreground and background emission and a constant relation between the 850 μm and the 8.3 μm dust opacities. This model assumes a constant dust temperature for all lines of sight. MSX and SCUBA data in direction of clear sub-mm sources were excluded from the fit, since these lines of sight have probably significantly higher dust temperatures. Figure 3 shows the trend for the 8.3 μm emission as a function of the 850 μm emission.

To measure more clearly the trend in the data, the solid line was calculated as the median 8.3 μm emission values within 15 bins of 0.02 Jy beam $^{-1}$. The error bars indicate the upper and lower quartiles. The dotted line indicates the best fitting model to the data.

For this dark cloud complex, a foreground emission of $(1.5 \pm 0.4) \times 10^{-6} \text{ W m}^{-2} \text{ sr}^{-1}$, a background emission of $(2.1 \pm 0.3) \times 10^{-6} \text{ W m}^{-2} \text{ sr}^{-1}$ and a mid to far IR ratio factor

PEAK VALUES					
Coordinates		Peak intensities		$\langle \tau_{8.3 \mu\text{m}} \rangle$	
R.A.	DEC	450 μm	850 μm		
[J2000]		[Jy beam ⁻¹]			
(1)	(2)	(3)	(4)	(5)	
P1	19 ^h 21 ^m 49.9 ^s	13°49′34.7″	3.08	0.531	0.3 ± 0.6
P2	19 ^h 21 ^m 47.0 ^s	13°49′22.7″	2.62	0.412	1.0 ± 0.6
EP	19 ^h 21 ^m 44.7 ^s	13°49′25.7″	1.55	0.314	1.3 ± 0.6

Table 2. 450 μm and 850 μm positions (Cols. 1–2) and peak intensities (Cols. 3–4) of P1, P2 and the extinction Peak. Column 5 lists the 8.3 μm optical depth as derived in Sect. 3.

of 5.2 ± 2.3 were found. This ratio is quite consistent with the value of 3.5 found for another IRDC (Johnstone et al., 2003). The authors noted that the ice mantle dust grains of Ossenkopf & Henning (1994) were more appropriate for the low mid to far IR ratio than the diffuse ISM grains of Draine & Lee (1984). This supports the choice of OH5 grains in Sect. 5.

Given an estimate of the foreground and background emission, a rough estimate for the 8.3 μm optical depth through the IRDC can be made. The 8.3 μm , MSX-beam averaged, optical depth can now be determined from the image via

$$\langle \tau_{8.3\mu\text{m}} \rangle = -\ln \frac{I - I_{\text{fg}}}{I_{\text{bg}}}. \quad (3)$$

Where I is the measured intensities from the MSX-map and I_{bg} and I_{fg} are estimated from the simple model fit.

4. Radial Profiles

The 450 μm and 850 μm data show three clear emission peaks (see Fig. 4). The emission peaks are labelled as P1, P2 and EP and the coordinates are listed in Table 2. Table 2 also indicates the brightness of the emission peaks and the estimated extinction as obtained from Eq. (3). The peak of MSX extinction (position EP) clearly corresponds to an 850 μm emission peak. At this position 450 μm also peaks, but it is not nearly as strong. In contrast, the other sub-mm emission peaks are strong at both 850 μm and 450 μm . Note that P1 lies at the edge of the MSX extinction structure, while P2 is well within the complex.

In order to model the emission, one dimensional radial profiles are constructed from the sub-mm data. Following the approach of Mueller et al. (2002), the sub-mm images are azimuthally averaged over relatively clean regions in the sub-mm images. In the sub-mm, the morphology of the IRDC is clearly present. For the radial averages, the general IRDC emission was avoided by choosing azimuthal angles for which a radial cut does not pass over other parts of the cloud.

Figures 5 and 6 show azimuthal averages around three positions, P1, P2 and the extinction Peak. A zero level correction was applied in all three cases. The choice of where to place the zero level is rather arbitrary. The impact of this choice was tested by modelling a much smaller radial cutoff (30′′) for P1. It was concluded that the main parameters of the modelling (enclosed mass and temperature structure) are independent of the choice of the radial extent.

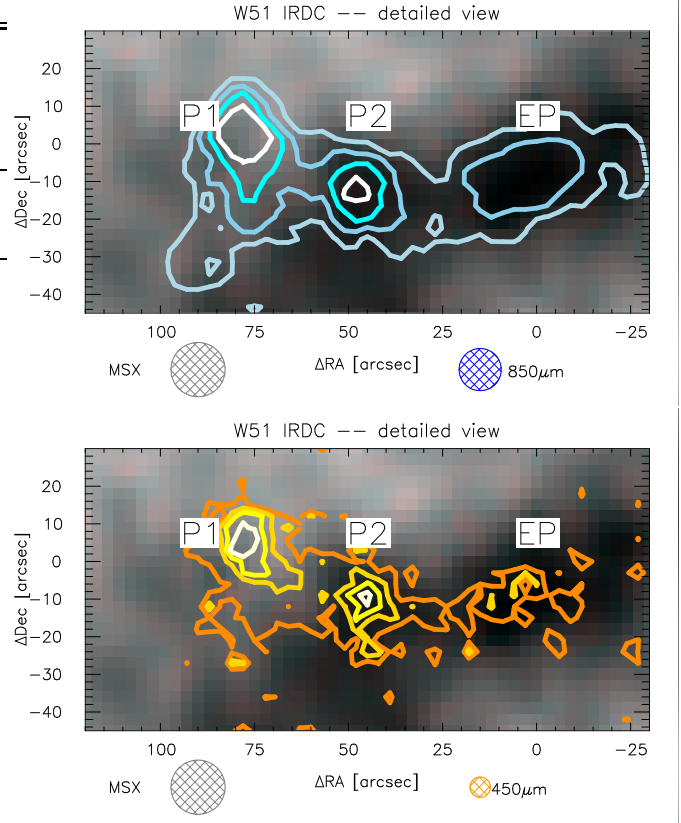


Fig. 4. Detailed view of the emission peaks, P1 and P2 and the EP at 450 μm (top) and 850 μm (bottom).

5. Core Model

Each position, P1, P2 and the extinction Peak is modelled as a spherical core with a density radial distribution which falls off as a power law. Internal heating sources are also considered as a possibility. The one dimensional diffusion code CSDUST3 of Egan et al. (1988) is used to calculate the continuum emission of each of the cores. Together with density power law exponent, the code requires a dust grain model, the optical depth through the core at one specified wavelength and the intensity of the interstellar radiation field.

CSDUST3 allows for a wide range of adjustable parameters. (A more exhaustive discussion on the code is given in appendix A.) For reasons of efficiency many of these parameters have been fixed throughout the modelling:

- Because the data shows all three cores as roughly circular, only spherical geometries were considered. Although on a larger scale the cores are part of an elongated extended structure, no attempt was made to incorporate this geometry in the modelling.
- The dust model of Ossenkopf & Henning (1994) (OH5 Col. 5) is used. This reflects a high density environment where intermediate ice-mantles might have formed. These opacities are consistent with the extinction analysis of Sect. 3. OH5 opacities are given in units of cm^2 per gram refractory material and the dust-to-hydrogen ratio of $1.5 \times 10^{-26} \text{ g H-atom}^{-1}$ (Draine & Lee, 1984) is applied to convert to units of cm^2 per hydrogen atom.

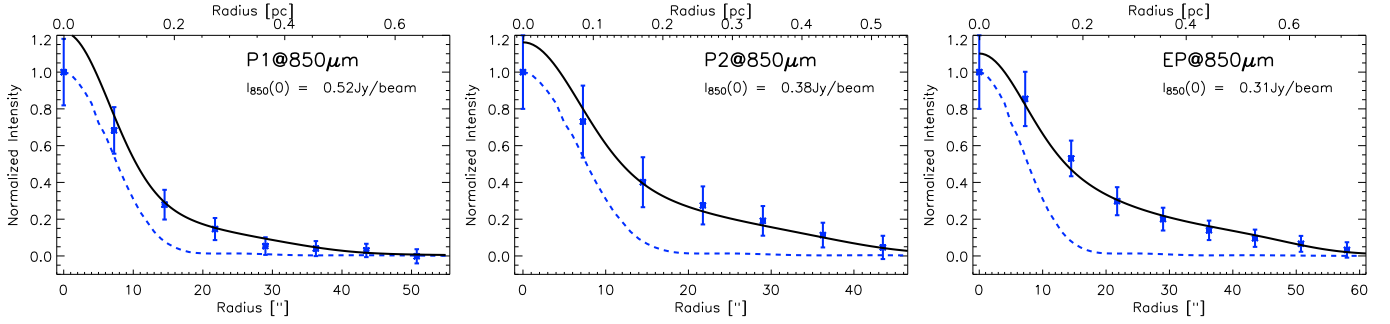


Fig. 5. 850 μm radial profiles of P1 (left panel), P2 (centre) and the extinction peak (EP, right). For each panel three features are shown. First the radially averaged data points, binned at every $1/2$ main beamwidth, where the radial averaging involves directions not contaminated by excess emission from e.g. neighbouring cores. These are normalised to their $r = 0''$ values. Secondly, the dashed line shows the Uranus beam profile, which is also normalised to its central value. Finally, the solid line gives the best fit to the data (see Table 3) with the same normalisation constant as the data.

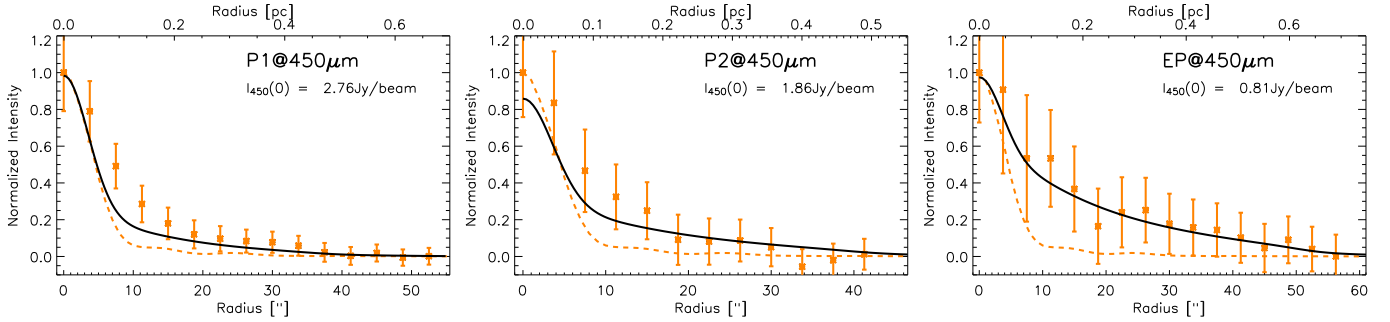


Fig. 6. Same as previous figure, but for the 450 μm data.

- The density distribution is cut-off at an inner cavity radius r_c . The radius of the cavity is chosen to be $r_c = 0.001 \text{ pc} = 206 \text{ AU}$ which is very small compared to the outer radius of the core ($\sim 1 \text{ pc}$). Hatchell & van der Tak (2003) conclude for similar modelling that their density distribution and resulting radial profiles are insensitive to the inner cavity radius used here.
- The wavelength grid consists of 60 points, distributed between $\lambda = 1 \mu\text{m}$ and $1300 \mu\text{m}$.
- The spatial grid consists of 100 points and is chosen to have a r^{-2} density of grid points. This density of grid point helps the convergence of the CSDUST3 code.
- The model makes use of a ‘reference frequency’ to which several parameters (e.g. opacity) are scaled (see App. A). 450 μm was chosen as the reference.
- Two primary choices for the Interstellar Radiation Field (ISRF) are that of Black (1994) and Mathis et al. (1983). A good comparison between these ISRFs is given by Zucconi et al. (2001). The Black ISRF is enhanced in the 10 – 50 μm range, leading to somewhat higher dust temperatures. Mathis et al. (1983) give the ISRF as a function of Galactocentric distance and their unattenuated ISRF at a Galactocentric distance of 6 kpc is used here. Furthermore, since the wavelength grid only starts from $\lambda = 1 \mu\text{m}$, the FIR and part of the NIR components have been left out. This is allowed, though, since only the cores are modelled, which lie well embedded within the molecular cloud. The choice, however, of the ISRF is not as significant as it would

seem. For the case of internal heating, the heating of the dense gas near the centre of the core is much more significant than the heating by the ISRF whereas for no internal heating the main impact is a poor estimate of the amount of emitting material.

- In the cases where internal heating was included, an effective temperature, T_{eff} , of this ‘heating’ has been fixed at 6500 K for all models. The CSDUST3 distributes all of the specified luminosity over the entire wavelength grid, with the relative distribution controlled by T_{eff} . A very high value of T_{eff} has no effect on the temperature structure, since the high energy photons are quickly re-radiated. Only if the effective temperature of the inner heating is low ($T \lesssim 30 \text{ K}$) will the radiation transport through the cloud be altered significantly.

After these specifications, 4 parameters remain free: *i*) the exponent of the density distribution p , *ii*) The optical depth at the reference frequency τ_{rod} , *iii*) the size of the cloud, i.e. the outer radius, R and *iv*) the luminosity of the heating source at its centre, L .

The first three combine to give the mass of the surrounding envelope

$$\mathcal{M} = 4\pi m_{\text{H}} \frac{\mu}{2} \frac{p-1}{3-p} \frac{\tau_{\text{rod}}}{\sigma_{\text{rod}}} \frac{1 - A_{\text{DR}}^{p-3}}{A_{\text{DR}}^{p-1} - 1} R^2 \quad (p \neq 1, 3), \quad (4)$$

where m_{H} is the mass of one hydrogen atom, $\mu/2 = 1.18$ the mean molecular weight per H-atom, σ_{rod} the opacity at 450 μm

and A_{DR} is the dynamic range, i.e., the ratio between the outer and inner radii. Because the mass of the envelope is as a physical quantity of more interest than the reference optical depth, \mathcal{M} was chosen as an input parameter and τ_{rod} was adjusted according to Eq. (4).

The output intensities of the model, as function of impact parameter were subsequently convolved with the approximated beam pattern of Table 1. For each set of parameters, a χ^2 goodness-of-fit was calculated

$$\chi^2 = \sum_{i(850)} \left(\frac{I_i - M_i}{\sigma_i} \right)^2 + \sum_{i(450)} \left(\frac{I_i - M_i}{\sigma_i} \right)^2 + \left(\frac{M_{100 \mu\text{m}}}{\sigma_{100 \mu\text{m}}} \right)^2 \quad (5)$$

with I the observed intensity, M the intensity of the model and σ_i the error in the observation. The respective contributions to the χ^2 denote respectively:

- The 450 μm and 850 μm profiles, which contribute multiple data points, separated by the main beams' half width.
- The IRAS non-detection, which adds an amount of $\left(\frac{M_{100 \mu\text{m}}}{\sigma_{100 \mu\text{m}}} \right)^2$ to the combined χ^2 . Here M_{100} is the model intensity at 100 μm convolved with an approximated IRAS beam (FWHM = 220'') and σ_{100} , the rms-noise in the IRAS map is set to $\sigma_{100} = 30 \text{ MJy sr}^{-1}$.

Finally, a beam convolved (FWHM = 18'') optical depth at 8.3 μm was calculated in order to compare the model results with the extinction map of MSX (but not used for the χ^2).

6. Results and Analysis

To find the minimum of the χ^2 in the 4-dimensional parameter space the problem is restated as an inverse problem for which solution (or retrieval) techniques are available (e.g. Rodgers, 2000). An iterative scheme was applied and the absolute minimum of χ^2 was usually found in a few iterations. Moreover χ^2 contour plots were made in which two parameters were varied (often the envelope's mass and source luminosity). In this way a good view on the χ^2 topology is obtained.

Table 3 gives for every profile (1st Col.) with corresponding cut-off radius (2nd Col.) the χ^2 minimum (7th Col.) and its location in the $(p, \mathcal{M}, \mathcal{D}, L)$ -plane (3rd – 6th Cols.). The errors in the parameters give the maximum range for which χ^2 increases by 1, with the remaining three parameters free to find their optimum values, i.e. minimising χ^2 . This $\Delta\chi^2$ behaves also as a χ^2 -distribution with one degree of freedom (Bevington & Robinson, 1992). The $\Delta\chi^2 = 1$ surface gives therefore the 1σ level of the parameters. Finally the MSX beam averaged model optical depth at 8.3 μm is given (8th Col.), which is a function of mass, density exponent and size.

Examples of χ^2 contour maps are given in Figs. 7 and 8. In Fig. 7 χ^2 contours are plotted (solid lines) as function of mass and luminosity at a fixed size and density exponent, while in Fig. 8 density exponent and luminosity are the varied parameters. Some general remarks about the χ^2 -mapping results can be stated:

- The IRAS detection limit, estimated at $3\sigma \approx 90 \text{ MJy sr}^{-1}$ corresponds roughly to luminosities of $L = 500 - 1000 L_{\odot}$,

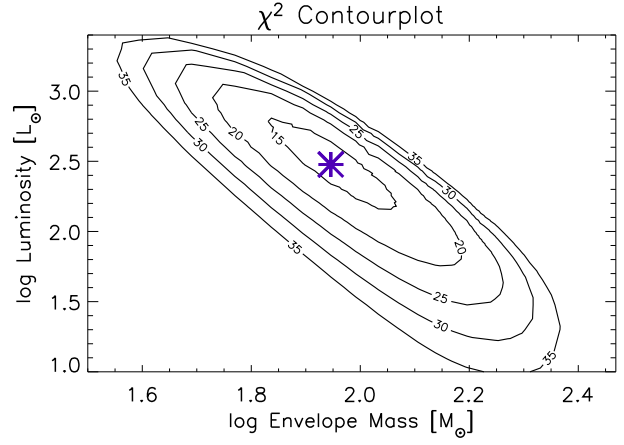


Fig. 7. χ^2 contour plot of the P1 model with $p = 2.25$ and a diameter of 75'' fixed. The solid lines indicate the value of χ^2 in the $\mathcal{M} - L$ plane. The elongated shape of the χ^2 contours is clearly visible and this illustrates a basic mass-luminosity degeneracy. The star indicates the χ^2 minimum which roughly corresponds to the parameters given in Table 3. See text for further discussion.

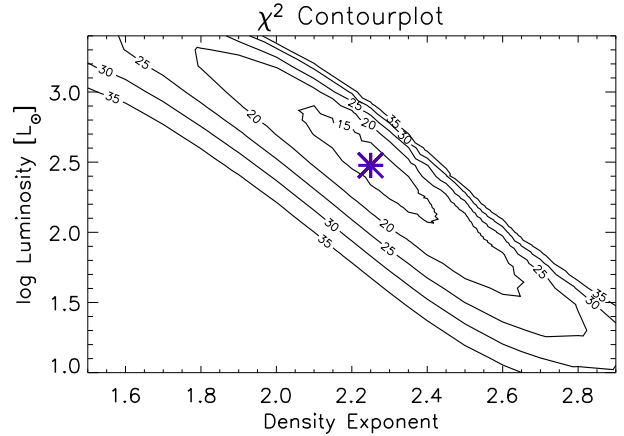


Fig. 8. Another contour plot of the P1 model, now at a fixed mass of $90 M_{\odot}$ and a diameter of 75''. The range in luminosity for which good fits ($\chi^2 < 15$) can be obtained spans almost one order of magnitude, while also the allowed range for the density exponent does not provide strong constraints.

only weakly depending on mass or density exponent. So with luminosities approaching $10^3 L_{\odot}$, the contribution of 100 μm to the total χ^2 becomes significant. This sets an upper limit for the luminosity of the source at the centre.

- For the P1 and P2 models a mass-luminosity degeneracy can clearly be observed. Figure 7 gives an example, where both a $\mathcal{M} = 130 M_{\odot}$, $L = 150 L_{\odot}$ -model and a $\mathcal{M} = 70 M_{\odot}$, $L = 600 L_{\odot}$ -model yield $\chi^2 = 15$. This mass-luminosity degeneracy is present in all of our results for the emission peaks. Note also that χ^2 is most sensitive to changes in \mathcal{M} .
- Apart from the $\mathcal{M} - L$ degeneracy other relations between the parameters can be observed. Shown in Fig. 8 is a $p - L$ contour plot at fixed mass ($\mathcal{M} = 90 M_{\odot}$) and size ($\mathcal{D} =$

MODEL RESULTS							
Profile ^a	r_{cut}	p	\mathcal{M}	\mathcal{D}^a	L	χ^2	$\langle\tau_{8.3\mu\text{m}}\rangle$
(1)	[$''$]	(3)	[M_{\odot}]	[$''$]	[L_{\odot}]	(7)	(8)
P1	55	$2.2^{+0.3}_{-0.2}$	91^{+25}_{-21}	73^{+10}_{-14}	330^{+370}_{-180}	12.6	0.53
P2	45	$2.0^{+0.3}_{-0.5}$	100^{+36}_{-22}	82^{+24}_{-16}	320^{+1000}_{-230}	5.4	0.55
EP	60	$2.2^{+0.3}_{-0.3}$	130^{+25}_{-24}	102^{+13}_{-13}	19^{+110}_{-17}	2.2	0.58

^a Diameter. A diameter of $30''$ corresponds to a linear radius of 0.196 pc.

Table 3. Results of the profiles that have been modelled. For every peak (Col. 1) cut-off radii (Col. 2) have been applied at which the profiles are zero-levelled. In Cols. 3 – 6 the most optimum values of p , \mathcal{M} , d and L are given for which χ^2 (Col. 7) is at its minimum. Indicated in the sub- and superscript of the parameters is the range of this parameter for which the χ^2 of Col. 7 increases by 1, indicating the 1σ -limits (see text for discussion). Finally the modelled beam-averaged $\tau_{8.3\mu\text{m}}$ (Col. 8) is given.

$75''$). Here the χ^2 is insensitive to an increase in p together with a decrease in L . This can be explained by putting more material nearer to the heating source. So, to keep χ^2 as it is, requires a lower internal luminosity for when material is closer to the source.

- For the extinction peak χ^2 levels are all very low. This is due to the large uncertainties that have been attributed to the $450\mu\text{m}$ profile, see Figs. 5 and 6. So for the extinction peak, the $850\mu\text{m}$ profile dominates the χ^2 -fitting.
- Another general point that can be stated is that the bulk of the χ^2 originates from the $450\mu\text{m}$ data. This can be seen either as an indication of poorer quality of the $450\mu\text{m}$ data or as higher information content. In the case of the $450\mu\text{m}$ data being of poorer quality than the $850\mu\text{m}$, it could be said that the uncertainties derived in the profiles are underestimated. On the other hand, it may be more difficult to model the $450\mu\text{m}$ profiles, because the data contain more information about the structure of the source than the spherical symmetric model allows.

7. Discussion

The density and temperature structures, as resulting from the best fit parameters are shown in Figs. 9 and 10. For the extinction peak temperatures have a minimum below 10 K within the envelope of the core. At the outer boundaries the temperature is set by the intensity of the ISRF and at the inner boundary by the $L = 19 L_{\odot}$ luminous source. The temperature structure follows the density profile in the sense that when the density gradient is high this also gives steep temperature gradients and – In case of a source – ensures high inner temperatures.

In Fig. 9 a model without inner heating is shown as well. This is interesting since the results for the extinction peak do not significantly rule out a model without heating. The lower 1σ luminosity limit of $1.7 L_{\odot}$ is sufficiently close to zero that a zero luminosity model will give a reasonable fit. The reason the model does prefer a source is to match the central $450\mu\text{m}$ data point of Fig. 6. For a zero luminosity model of the extinction peak, the temperature drops even further, below 5 K (the core-model does not account for gamma-ray heating), while as

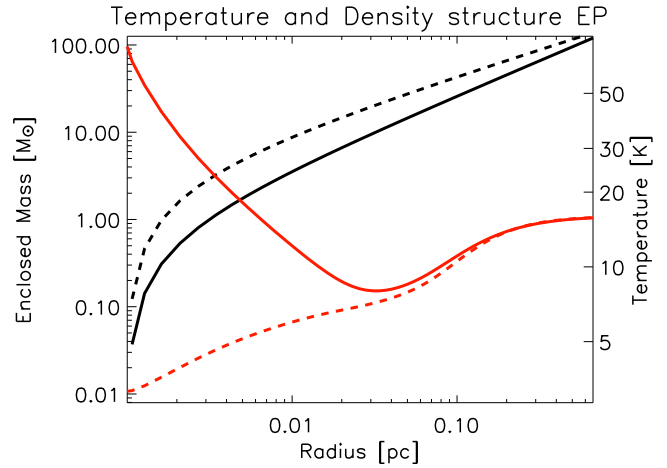


Fig. 9. The Solid lines give the temperature (orange) and density (black) structure of the minimum χ^2 model of Table 3 for the extinction peak. This shows temperatures dropping below 10 K within the envelope, but rising toward the boundaries through the heating of ISRF and the $19 L_{\odot}$ source respectively. The dashed line represents a model without inner heating ($L = 0$). Here, temperatures drop below 5 K and densities are higher to compensate for the lower temperature. The χ^2 of this model is 4.5.

a compensating factor for the lack of a source the density is increased.

The temperature structures for the emission peaks are comparable to each other (Fig. 10). This is also to be expected, since the central luminosities are roughly the same ($L \approx 300 L_{\odot}$). Although the mass of P2 is calculated to be higher than that of P1, P1's steeper density distribution puts more mass in the inner regions, which is also reflected in the temperature structure; P1 does more resemble a point source. Hatchell & van der Tak (2003), who modelled high-mass star-forming cores, find somewhat less steep density distributions, although given the uncertainties, the findings do still agree.

Col. 8 of Table 3 shows the MSX-beam convolved $8.3\mu\text{m}$ optical depth that results from the density distribution of the core-model. This can be compared with the findings of Sect. 3. It is expected that the observed opacity at $8.3\mu\text{m}$ is higher since the modelling deals with the cores only. This is indeed the case

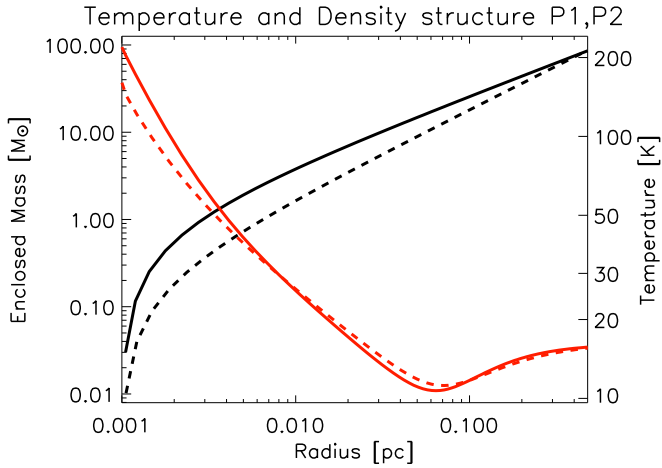


Fig. 10. The temperature (orange) and density (black) structure for the minimum χ^2 model of P1 (solid lines) and P2 (dashed lines) respectively, which parameters are given in Table 3.

for P2 and the extinction peak, but P1, on the other hand, is an exception. Although the core-modelling tells that it must be similar to e.g. P2 at $8.3 \mu\text{m}$, this is not reflected in MSX. Here, P1, unlike P2 and EP, does not fall within the main S-shaped extinction valley. Moreover, the source luminosity is not high enough to fill in the missing $8.3 \mu\text{m}$ emission (a $10^5 L_{\odot}$ is needed). Possible answers are a non-spherical geometry for P1 or a non-smooth distribution of the material. This latter suggestion, in which the clumpy material lowers the beam averaged opacity, will be investigated in a subsequent paper.

One of the key question of this research was whether internal heating is present within the IRDC cores. This can now be answered conclusively for the emission peaks, but is still unclear for the extinction peak. Although the models certainly prefer a source, the uncertainties do not discount a source free core. Essentially there is a $p - L$ degeneracy (see Fig. 8); the presence of a possible source can be ‘hidden’ by the model by reverting to a steep density profile. Future modelling of e.g. molecular lines or the inclusion of additional mid IR continuum data into the core-model will have to decide whether or not a source is present.

The results for the emission peaks, on the other hand, point very convincingly to the presence of sources, although their luminosities are poorly constrained and can be easily off by one order of magnitude. The core model does not constrain the nature of the sources, though with luminosities of hundreds of solar units, it is hard to think of anything but stellar. Pre main-sequence evolution tracks of Palla & Stahler (1999) show $300 L_{\odot}$ luminous sources correspond to masses in the range of $M \approx 3 - 5 M_{\odot}$, only slightly depending on the evolutionary stage. This corresponds to intermediate mass star formation and the spectral type would be late B. However, since star formation in general is not a lonely process, multiple stars might have formed, which might change this analysis, although it is often the star of highest mass that produces the bulk of the luminosity.

8. Conclusion and further work

We summarise the main conclusions of this research

- Through self-consistent modelling of dust emission the presence of warm material embedded in a surrounding envelope is identified for the cores P1 and P2. While the nature of this heating is still unresolved, the energy involved should be at least a few hundreds of solar luminosities. For the extinction peak the presence of a source is not settled, although the models seem to prefer it.
- Assuming a stellar nature for the P1 and P2 sources, luminosities of about $300 L_{\odot}$ are equivalent to main sequence stars between B5 and B8.
- The envelope’s masses are in the order of $70 - 150 M_{\odot}$, only slightly depending on the assumed density distribution. The density exponent is constrained to be $p \approx 2.0$ for all cores. The density gradient correlates with the temperature structures, such that steep gradients result in more extreme values for the temperature near the inner cavity.
- The $8.3 \mu\text{m}$ extinction as derived from the model corresponds well with the extinction derived from MSX, except for P1, whose lack of $8.3 \mu\text{m}$ extinction in MSX is not in accordance with the model results. This results might be explained by a geometry effect (i.e. the spherical geometry fails) or by a non-smooth density distribution.
- With the dust density and temperature structure, detailed modelling of line emission from the cores will be possible. Such efforts can place more constraints on the nature of the cores and potentially place the cores in an evolutionary context (van Dishoeck & Blake, 1998).

Future work will focus on the dynamics of the IRDC-cores and will involve the modelling of molecular line transitions. Already a wide survey of molecular species and transitions has been gathered, from JCMT and KOSMA² observations. The aim of the line observations is to determine the velocity structure of the IRDC complex and whether the velocity structure is thermal or turbulent in nature. Answers to these questions, together with the result of this research, might provide clues to the evolutionary state of these cores – How the cores individually relate to one another and how they fit in the canonical scheme of (intermediate mass) star formation.

Acknowledgements. This research made use of data products from the Midcourse Space Experiment. Processing of the data was funded by the Ballistic Missile Defense Organization with additional support from NASA Office of Space Science. This research has also made use of the NASA/ IPAC Infrared Science Archive, which is operated by the Jet Propulsion Laboratory, California Institute of Technology, under contract with the National Aeronautics and Space Administration.

References

- Bevington, P. R. & Robinson, D. K. 1992, 319–+
 Black, J. H. 1994, in ASP Conf. Ser. 58: The First Symposium on the Infrared Cirrus and Diffuse Interstellar Clouds, 355–+
 Boersma, C. 2003, in <http://www.astro.rug.nl/~boersma/YELLOW/FILES/ko.ps>

² Kölner Observatorium für Sub-Millimeter Astronomie

- Carey, S. J., Clark, F. O., Egan, M. P., et al. 1998, *ApJ*, 508, 721
- Carey, S. J., Feldman, P. A., Redman, R. O., et al. 2000, *ApJ*, 543, L157
- Draine, B. T. & Lee, H. M. 1984, *ApJ*, 285, 89
- Egan, M. P., Carey, S. J., Price, S. D., et al. 1999, in *ESA SP-427: The Universe as Seen by ISO*, 671–+
- Egan, M. P., Leung, C. M., & Spagna, G. F. 1988, *Computer Physics Communications*, 48, 271
- Egan, M. P., Shipman, R. F., Price, S. D., et al. 1998, *ApJ*, 494, L199+
- Evans, N. J., Rawlings, J. M. C., Shirley, Y. L., & Mundy, L. G. 2001, *ApJ*, 557, 193
- Hatchell, J. & van der Tak, F. F. S. 2003, *A&A*, 409, 589
- Jenness, T., Holland, W. S., Chapin, E., Lightfoot, J. F., & Duncan, W. D. 2000, in *ASP Conf. Ser. 216: Astronomical Data Analysis Software and Systems IX*, 559–+
- Jenness, T. & Lightfoot, J. F. 1998, in *ASP Conf. Ser. 145: Astronomical Data Analysis Software and Systems VII*, 216–+
- Johnstone, D., Fiege, J. D., Redman, R. O., Feldman, P. A., & Carey, S. J. 2003, *ApJ*, 588, L37
- Leung, C. M. 1975, *ApJ*, 199, 340
- Mathis, J. S., Mezger, P. G., & Panagia, N. 1983, *A&A*, 128, 212
- Mueller, K. E., Shirley, Y. L., Evans, N. J., & Jacobson, H. R. 2002, *ApJS*, 143, 469
- Ossenkopf, V. & Henning, T. 1994, *A&A*, 291, 943
- Palla, F. & Stahler, S. W. 1999, *ApJ*, 525, 772
- Péroult, M., Omont, A., Simon, G., et al. 1996, *A&A*, 315, L165
- Press, W. H., Teukolsky, S. A., Vetterling, W. T., & Flannery, B. P. 1992, *Numerical recipes in FORTRAN. The art of scientific computing* (Cambridge: University Press, —c1992, 2nd ed.)
- Price, S. D., Egan, M. P., Carey, S. J., Mizuno, D. R., & Kuchar, T. A. 2001, *AJ*, 121, 2819
- Redman, R. O., Feldman, P. A., Wyrowski, F., et al. 2003, *ApJ*, 586, 1127
- Rodgers, C. D. 2000, in *Series on Atmospheric, Oceanic and Planetary Physics*, 256–+
- Shirley, Y. L., Evans, N. J., & Rawlings, J. M. C. 2002, *ApJ*, 575, 337
- Shirley, Y. L., Evans, N. J., Rawlings, J. M. C., & Gregersen, E. M. 2000, *ApJS*, 131, 249
- Teyssier, D., Hennebelle, P., & Péroult, M. 2002, *A&A*, 382, 624
- van der Tak, F. F. S., van Dishoeck, E. F., Evans, N. J., & Blake, G. A. 2000, *ApJ*, 537, 283
- van Dishoeck, E. F. & Blake, G. A. 1998, *ARA&A*, 36, 317
- Wouterloot, J. G. A. & Brand, J. 1989, *A&A*, 80, 149
- Zucconi, A., Walmsley, C. M., & Galli, D. 2001, *A&A*, 376, 650

Appendix A: Description of CSDUST3

The `csdust3` diffusion code is the code from Egan et al. (1988) and for a thorough discussion of the code the reader is referred to this article. The theoretical background, of which here only a short summary is given, is dealt with in depth in Leung (1975). Another description of `csdust3` is given by Boersma (2003) in his small research project thesis. We only consider spherical symmetry.

The zeroth and first moment equation of radiative balance are: (Leung, 1975)

$$\frac{1}{r^2} \frac{\partial}{\partial r} (r^2 H_\nu(r)) = -\sigma_\nu^a(r) (J_\nu(r) - B_\nu(r)) \quad (\text{A.1})$$

$$\frac{\partial K_\nu(r)}{\partial r} + \frac{3K_\nu(r) - J_\nu(r)}{r} = -\kappa_\nu H_\nu(r) \quad (\text{A.2})$$

In which r is the radial coordinate, $H_\nu(r)$ the Eddington flux at frequency ν , $\kappa_\nu = (\sigma_\nu^a(r) + (1 - \frac{1}{3} a_1) \sigma_\nu^s(r))$ the extinction coefficient, $J_\nu(r)$ the mean intensity, $B_\nu(r)$ the Planck function, $K_\nu(r)$ the ‘K-integral’ (i.e. the second moment of intensity), σ_ν^a the absorption coefficient, a_1 the first Legendre coefficient and σ_ν^s the scattering coefficient. Equation (A.2) can be rewritten as

$$\frac{\partial}{\partial r} (f_\nu \zeta_\nu J_\nu) = -\kappa_\nu \zeta_\nu H_\nu, \quad (\text{A.3})$$

where the anisotropy factor, $f_\nu(r)$, has been defined as $f_\nu(r) \equiv \frac{K_\nu(r)}{J_\nu(r)}$ and the configuration factor, ζ_ν , is chosen such that Eq. (A.3) is valid.³ At the boundary (i.e. at $r = r_c$ and $r = R$) boundary values are defined as $f_\nu^B \equiv \frac{H_\nu^+ + H_\nu^-}{J_\nu}$ with $H_\nu \equiv H_\nu^+ - H_\nu^-$. At the inner and outer radius Eq. (A.3) with these definitions becomes

$$\begin{aligned} \frac{\partial}{\partial r} (f_\nu \zeta_\nu J_\nu) &= \kappa_\nu \zeta_\nu (2H^- - f_\nu^B J_\nu) \text{ at } r = R \\ &= \kappa_\nu \zeta_\nu (f_\nu^C J_\nu - 2H^+) \text{ at } r = r_c \end{aligned}$$

Equation (A.3) together with Eq. (A.1) combine to give

$$\frac{\partial}{\partial r} \left(\frac{r^2}{\kappa_\nu \zeta_\nu} \frac{\partial}{\partial r} (f_\nu \zeta_\nu J_\nu) \right) = r^2 (\sigma_\nu J_\nu - \epsilon_\nu) \quad (\text{A.5})$$

with $\epsilon_\nu = \sigma_\nu^a B_\nu(T)$. This is the equation of radiative balance and together with the equation of energy balance,

$$\int dv (\epsilon_\nu(r) - \sigma(r) J(r)) = 0, \quad (\text{A.6})$$

the dust temperature distribution can be computed at every r . This is first done in the diffusion approximation ($f = \frac{1}{3}$, $f^B = f^C = \frac{1}{2}$, $\zeta = 1$). From the resulting temperature distribution the angular distribution of the radiation field is computed using a ray-tracing technique (as explained in Leung

³ This means that for planar geometry $\zeta = 1$. For spherical geometries, though, the configuration factor must be defined

$$\zeta_\nu(r) \equiv \exp \left[\int_0^r \frac{dx}{x} \left(3 - \frac{1}{f_\nu(x)} \right) \right]. \quad (\text{A.4})$$

(1975)). This gives $f(r)$, f^B , f^C , $\zeta(r)$ and the temperature distribution for the next iteration is again computed from Eq. (A.5) and Eq. (A.6). Naturally `csdust3` works with dimensionless equivalents of these equations.

Equation (A.5) and Eq. (A.6) contain parameters that must be fixed, most notably the extinction, κ_ν , and absorption σ_ν^a coefficients. This is determined by the density distribution, i.e. by the *size* (inner and outer radii, r_c , R), density exponent⁴, p , the dust model and an optical depth at a reference frequency,

$$\tau_{\text{rod}} = \int_{r_c}^R dr \sigma_{\text{rod}}^a n_c \left(\frac{r}{r_c} \right)^{-p}, \quad (\text{A.7})$$

which sets the absolute density scale (n_c). Note however that the reference optical depth is just a model parameter and is not very appropriate in making physical or observational comparisons. More suitable is the envelopes mass,

$$\mathcal{M} = m_{\text{H}} \int_{r_c}^R dr 4\pi r^2 n_c \left(\frac{r}{r_c} \right)^{-p}, \quad (\text{A.8})$$

which is subsequently used as an input parameter and converted to τ_{rod} via Eq. (4), which follows directly from integrating Eq. (A.7) and Eq. (A.8). The dust model provides at every wavelength the total extinction, the absorption and scattering cross sections through the albedo and the asymmetry parameter, $g = \frac{1}{3} a_1$. It is possible to provide multiple dust models.

Other input variables that should be fixed are the incident fluxes at the clouds inner ($H_\nu^+(r_c)$) and outer ($H_\nu^-(R)$) boundary. The former is only nonzero if a source is present and is defined via the luminosity (of this source) and the effective temperature. The flux incident on the cloud is determined by providing an external radiation field, J_ν^{ext} . This is most naturally the interstellar radiation field.

`csdust3` calculates the emergent intensities as function of impact parameter, ξ . For an observational comparison it is for possible, given a $\sigma = \frac{\text{FWHM}}{2.35}$ of the (main) beam, to provide convolved intensities. The convolution integral in its most general form is

$$I_{\text{cv}}(x_0, y_0) = \frac{1}{2\pi\sigma^2} \int dx dy I(x, y) \exp \left[-\frac{(x - x_0)^2 + (y - y_0)^2}{2\sigma^2} \right]. \quad (\text{A.9})$$

Where x and y are Cartesian coordinates in the image plane of the observer and $I_{\text{cv}}(x_0, y_0)$ is the convolved intensity, the observer would witness. However `csdust` computes these ‘convolution maps’ only for a modest amount of impact parameters. Therefore it was chosen to implement the convolution manually. Since through spherical symmetry $I(x, y)$ depends on one impact parameter only, i.e. $I(x, y) = I(\sqrt{x^2 + y^2}) \equiv I(\xi)$, I_{cv} can also be specified by one parameter only, so $I_{\text{cv}}(\xi_0) \equiv I_{\text{cv}}(x_0, 0)$. A change to spherical variables (ξ, θ) then gives:

$$I_{\text{cv}}(\xi_0) = \frac{1}{2\pi\sigma^2} \int d\xi \xi \exp \left[-\frac{1}{2\sigma^2} (\xi - \xi_0)^2 \right] B(\xi, \xi_0) I(\xi). \quad (\text{A.10})$$

⁴ Gaussian density distributions are also possible.

Where $B(\xi, \xi_0)$ involves the angular part of the integration

$$B(\xi, \xi_0) = \int_0^{2\pi} d\theta \exp\left[-\xi_0 \xi (1 - \cos(\theta)) / \sigma^2\right] \quad (\text{A.11})$$

$$= 2 \int_0^\pi d\theta \exp\left[-\xi_0 \xi (1 - \cos(\theta)) / \sigma^2\right], \quad (\text{A.12})$$

by symmetry. Expression A.12 is numerically convenient, since the argument of the exponent is always negative.^{5, 6}

Appendix B: The Retrieval technique

The retrieval technique essentially is an extension of Newton's 1d method in finding solutions for numerical problems. More generally we can think of a system of m functions (or measurements) depending on n arguments. The solution to this problem, $\mathbf{y} = F(\mathbf{x})$, maps the arguments vector, \mathbf{x} (n -elements), to the solutions (i.e. measurements), \mathbf{y} of m elements.

The model, M , maps any set of arguments to the corresponding model values, e.g. $\mathbf{y}_0 = M(\mathbf{x}_0)$. In this example \mathbf{x}_0 is a first guess for the arguments, that corresponds via the model to a set of values, \mathbf{y}_0 , which will differ from the 'true' measurements, \mathbf{y} . A first order Taylor approximation around the guess-point, \mathbf{x}_0 then gives

$$\mathbf{y} - \mathbf{y}_0 = \mathbf{K}(\mathbf{x} - \mathbf{x}_0) \quad (\text{B.1})$$

Where $\mathbf{K} = K[n, m]$ is a $n \times m$ first-derivative matrix, measuring the increase of every m -element of \mathbf{y}_0 to every argument n , i.e.⁷

$$K[n, m] = \frac{M(\mathbf{x}_0 + \Delta x_0(n))[m] - M(\mathbf{x}_0)[m]}{\Delta x_0(n)}. \quad (\text{B.2})$$

Equation B.1 is a first-order approximation and solving for \mathbf{x} yields a new, and – hopefully better – guess of the model-arguments. Solving for \mathbf{x} in Eq. (B.1) yields the iterative scheme

$$\mathbf{x}_{k+1} = \mathbf{x}_k + (\mathbf{K}^T \mathbf{K})^{-1} \mathbf{K}^T (\mathbf{y} - \mathbf{y}_k). \quad (\text{B.3})$$

For these techniques to be applicable the quantity of interest is not the scalar χ^2 but rather the vector

$$\mathbf{y} = \frac{\mathbf{I}^{\text{obs}} - \mathbf{I}^{\text{cv}}(\mathbf{x})}{\sigma}, \quad (\text{B.4})$$

i.e. the difference of the observations with the model results, divided by the error in the observations. The retrieval technique then tries to find the model parameters, \mathbf{x} , for which \mathbf{y}

⁵ which is also the case for A.10. That is the reason the argument of the exponent is written in this form rather than simply $-(\xi^2 - 2\xi\xi_0 \cos(\theta) + \xi_0^2) / 2\sigma^2$.

⁶ Note also that $B(\xi, \xi_0)$ can be expressed in the modified Bessel function of first order, I_0 ,

$$B(\xi, \xi_0) = 2\pi \exp\left[\left(-\frac{\xi\xi_0}{\sigma^2}\right)\right] I_0\left(\frac{\xi\xi_0}{\sigma^2}\right). \quad (\text{A.13})$$

⁷ This notation might be confusing. What is e.g. meant with $M(\mathbf{x}_0 + \Delta x_0(n))[m]$ is to increase the n^{th} -element of the argument vector, \mathbf{x}_0 , with an amount Δx_0 , and take the m^{th} component from the results vector (i.e. the values the model returns).

is zero via the procedure described above. This will not succeed in general, but the iterative scheme will yield solutions for which $\chi^2 = \|\mathbf{y}\|^2$ is minimised. For computational reasons, we limit the maximum increase of each particular argument by a factor 2 in log space. This is required, since shallow gradients near \mathbf{x}_k can easily pull the next iteration far away. Moreover we assure that the next iteration is indeed an improvement in χ^2 . And finally we performed our calculation in log-space, to better reflect the exponential nature of the argument and also because negative solution do not play a role.

The retrieval technique converges quite rapidly to the minimum of χ^2 . The drawback, though, is that the exact position the technique converges to, is somewhat dependent on initial condition. This can be remedied by computing the minimum for different initial condition, thereby introducing an element of randomness (in those initial conditions). To be absolutely sure of the χ^2 minimum this is followed up a downhill-simplex approach (Press et al., 1992), which tries to improve on the absolute minimum, by slowly confining the N -dimensional area spanned by its input parameters around the χ^2 minimum.

III. HCO⁺ line modelling

of IRDC cores

HCO⁺ Line modelling of InfraRed Dark Cloud Cores

C.W. Ormel¹, V. Ossenkopf^{2,3}, F.P. Helmich^{1,2}, and R.F. Shipman^{1,2}

¹ Kapteyn Astronomical Institute, PO box 800, 9700 AV Groningen, The Netherlands
e-mail: ormel@astro.rug.nl

² SRON National Institute for Space Research, Landleven 12, 9747 AV Groningen, The Netherlands
e-mail: russ@sron.rug.nl
e-mail: f.p.helmich@sron.rug.nl

³ i. Physikalisches Institut, Universität zu Köln, Zùlpicher Straße 77, 50937 Köln, Germany
e-mail: ossk@ph1.uni-koeln.de

Abstract. From dust continuum modelling a rough indication of the density and temperature structure of three individual cores within the W51-IRDC was obtained. Two of them were found to harbour a $L \gtrsim 100 L_{\odot}$ source, while the third did not require such a source for the data to be modelled. Here, the modelling is extended to molecular lines, of which HCO⁺ is treated as a pilot, but which could be easily extended to other molecules. The model is capable in taking into account effects of turbulent clumping, which reduces the effective opacity. Observations from the KOSMA telescopes show the presence of extended emission, which is incorporated into the model. The fitting of the JCMT observations is then restricted to four parameters. We find HCO⁺ abundances in the order of 10^{-9} for both cores. The volume filling factors though differ, which might reflect a different stage of fragmentation. Finally, for the turbulent velocity distributions, negative radial exponents were found, indicative of star formation activity.

1. Introduction

Molecular lines have been used to probe the physical and chemical structure of molecular clouds. Molecules are collisionally excited in their low energy rotational levels and radiate in the sub-mm. The CO molecule, for example, which is found in high abundances throughout the ISM, is often used in such occasions. In this report we will focus on HCO⁺, a high density tracer, less vulnerable to freeze-out and for which we have obtained data with both JCMT¹ and KOSMA² telescopes, sufficiently strong to be modelled.

H₂CO line observations of Infra Red Dark Clouds (IRDCs) have been made by Carey et al. (1998) in order to probe dense gas, which was followed up by continuum observations. Their analysis involved a Large Velocity Gradient (LVG) model to constrain the excitation conditions, which showed densities in excess of $n > 10^5 \text{ cm}^{-3}$ and temperatures below 20 K. Moreover Carey et al. (2000) observed several cores in HCO⁺ and found strong, asymmetric profiles, characteristic of in-

falling material. In this paper JCMT observations are combined with a sophisticated line radiative transfer model which includes the effects of turbulent-clumping. As e.g. van der Tak et al. (1999) and Ossenkopf et al. (2001) already noted, detailed radiative transfer better reflect the detailed physical structure than analytic approximations or escape probability models do.

The lay-out of this paper is as follows: In Sect. 2 a (theoretical) introduction to line-formation in general and that of HCO⁺ in particular is given. The aim is to understand the physical processes behind the characteristics of the line profile. What are e.g. the specific imprints of the density and temperature structure, turbulence, infall, etc. on the profile? And how do these affect the convolved profile as seen by the JCMT and KOSMA telescopes?

All modelled line profiles in this report are created with SIMLINE (see Sect. 2.3), a one-dimensional code which is unique in taking into account turbulent clumping. Depending on the specific type of turbulent-clumping, a significant decrease in opacity can be reached (Sect. 2.2, Eq. 19), while in Sect. 2.4 synthetic profiles are presented and discussed.

Section 3 deals with the modelling of the observations in a similar way as is done for the continuum, i.e. by minimizing the χ^2 goodness-of-fit parameter (see Paper I). Here we decide on parameters that can be fixed and limit the number of parameters to be varied to four. Two cores, P1 and EP are modelled and their results are discussed in Sect. 3.5.

¹ The JCMT is operated by the Joint Astronomy Centre in Hilo, Hawaii on behalf of the parent organizations Particle Physics and Astronomy Research Council in the United Kingdom, the National Research Council of Canada and The Netherlands Organization for Scientific Research.

² The KOSMA 3m radiotelescope at Gornergrat-Süd Observatory is operated by the University of Cologne and supported by special funding from the Land NRW. The Observatory is administered by the Internationale Stiftung Hochalpine Forschungsstationen Jungfrauoch und Gornergrat, Bern.

THE HCO ⁺ MOLECULE					
molecule	transition	Frequency [GHz]	E_{upper} [K]	A_{ul} [s ⁻¹]	n_{crit}^a [cm ⁻³]
CO	2→1	230.5	16.6	6.91×10^{-7}	$(1.4 - 2.5) \times 10^4$
	3→2	345.8	33.2	2.50×10^{-6}	$(4.1 - 10.0) \times 10^4$
HCO ⁺	3→2	267.6	25.7	1.46×10^{-3}	$(3.7 - 4.0) \times 10^6$
	4→3	356.7	42.8	3.60×10^{-3}	$(9.5 - 9.7) \times 10^6$
CS	5→4	244.9	35.3	2.97×10^{-4}	$(8.0 - 11.8) \times 10^6$
	7→6	342.9	65.8	8.36×10^{-4}	$(2.9 - 4.9) \times 10^7$

^a Quoted ranges correspond to temperatures varying from 10K to 40K

Table 1. Properties of some frequently used molecular tracers for probing (dense) molecular clouds.

2. The formation of line profiles

2.1. Molecular Properties

Since HCO⁺ possesses a large dipole moment μ , this naturally gives high values for the Einstein-A coefficient,

$$A_{\text{ul}} = \frac{64\pi^4\nu^3\mu^2}{3c^3h} f_{\text{ul}}, \quad (1)$$

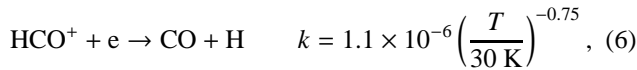
(f_{ul} is the transition strength) and subsequently leads to high emission coefficients, $j_\nu \propto A_{\text{ul}}$, making HCO⁺ easily radiate. The consequence, though, of the high Einstein-A, is that the molecule is difficult to excite in low density environments. In fact the critical density,

$$n_{\text{crit}} = \frac{A_{\text{ul}}}{\sum_{i \neq u} K_{\text{ui}}}, \quad (2)$$

(where the K_{ui} are the collision rate coefficients involving the upper level) makes the HCO⁺ molecule together with molecules as CS and HCN an important tracer of high densities (see Table 1). Because of its dipole, it is rapidly formed through ion-molecule reactions for which also no activation energy is required:³



In cold, dense cores CO⁺ (lack of ionizing photons) and H₂O (frozen out) are less important, so it is the latter reaction by which HCO⁺ is formed. In Photon Dominated Regions (PDRs), characterised by high electron fractions, destruction goes through electron recombination, i.e.



but in cold molecular clouds again the ion-molecule reactions are dominant



³ All rate coefficients, k , quoted here are from Tielens (2003) with units in cm³ s⁻¹. If the reaction reads $A + B \rightarrow C + D$, then the product of k with the concentration of A and B, $k[A][B]$, determines the rate at which C and D are formed. For ion-molecule reactions k does not have a temperature dependence. Otherwise this is indicated.

where M represents a wide possibility of (complex) neutral molecules. Therefore no simple relation of the HCO⁺ abundance with other species can be drawn; a full chemical model – beyond the scope of this article – would have to be run. However, the strength of the HCO⁺ lines make this molecule easily observable, provided regions of high enough density are probed. HCO⁺ moreover does not suffer severely from freeze-out, since ions do not stick easily on grains. Subsequently HCO⁺ is very appropriate to model the physical structure as well as the turbulent velocity structure of cold cloud cores.

2.2. The turbulence description

Turbulent motion occurs when the internal velocity of the system is higher than the thermal velocity dispersion (σ_{th}) as given by the kinetic temperature of the molecules. In the statistical turbulent approximation – as originated by Martin et al. (1984) and which SIMLINE uses – the intrinsic nature of turbulence is of little importance. The model assumes a distribution of clumps (or fragments), whose mutual velocity distribution is turbulent (σ), but with a thermal distribution of velocities within each single fragment. The model is capable in producing all turbulent-clumping types: *micro-turbulence* (turbulence without clumping), *incompressible turbulence* (where the clumping only occurs in velocity space) and *compressible turbulence*, where clumping is also in real, physical space.

Incompressible turbulence means that within one line of sight the velocity structure shows an irregular structure, preferring particular velocities. On the whole the velocity distribution is given by σ and smooth, but locally it is clumped on scales of σ_{th} . Let the clump velocity be v_i and its peak density, i.e. the density of molecules *moving* at v_i , be n_0 . For the spatial distribution of molecules moving at that velocity, a Gaussian density distribution is customary and still physically reasonable. So,

$$n(r) = n_0 \exp \left[- \left(\frac{r}{r_{\text{cl}}} \right)^2 \right], \quad (8)$$

is the density of molecules moving at v_i within a thermal width. This is what is called ‘coherent unit’ or fragment in the remainder of this section. Integrating Eq. (8) the volume of the fragments, V_{frag} , as defined in

$$\int_0^\infty dr 4\pi r^2 n(r) \equiv V_{\text{frag}} \times n_0, \quad (9)$$

equals $\pi^{3/2} r_{\text{cl}}^3$. So if r_{cl} becomes large, the fragments are large, which is a measure of the amount of clumpiness.

More generally one can think of fragments with a varying optical depth $\tau(x, y)$ as function of the coordinates in the observers plane. Here $\tau(x, y)$ is the peak optical depth as measured at $v_z = v_i$ and its velocity dependence is then given by,⁴

$$\exp\left[-\pi\left(\frac{v_i - v_z}{\sigma_{\text{th}}}\right)^2\right], \quad (10)$$

where the observer measures at v_z . The effective optical depth in the limit of an infinite number of identical fragments can be shown to be (Martin et al., 1984)

$$\tau_{\text{eff}} = \Delta N_i \int_A dx dy (1 - e^{-\tau(x, y)}). \quad (11)$$

In which ΔN_i is the column density of fragments, A the area of the fragment over which is integrated and the notion ‘effective optical depth’ implies $e^{-\tau(x, y)}$ has been averaged, since $e^{-\tau}$ rather than τ itself is of importance in the radiative transfer transport. Equation (11) shows that the contribution to the effective optical depth of area element $dx dy$ involves a weighting factor $(1 - e^{-\tau})$. If $\tau \ll 1$ this increases linearly with τ , as expected in optically thin cases, whereas if $\tau \gg 1$ the weighting factor stays 1 and the dependence on τ vanishes, though τ_{eff} can still grow in areas within A being not yet opaque. Alternatively the integral in Eq. (11) can be thought of as the effective opaque area of the single fragment.

Since $n(r)$ is related to $\tau(x, y)$, Eq. (11) can be integrated (using some handy change of variables)⁵

$$\tau_{\text{eff}} = \Delta N_i \pi r_{\text{cl}}^2 \int_0^{\tau_{\text{cl}}} \frac{d\tau}{\tau} (1 - e^{-\tau}). \quad (13)$$

In which $\tau_{\text{cl}} = \kappa r_{\text{cl}} \sqrt{\pi}/\sigma_{\text{th}}$ is the central (peak) optical depth in a clump and κ the frequency integrated opacity of the fragment at a density n_0 as defined in

$$\kappa(v; \sigma_{\text{th}}) \equiv \kappa \Phi(v) \equiv \kappa \frac{1}{\sigma_{\text{th}}} \exp\left[-\pi(v/\sigma_{\text{th}})^2\right]. \quad (14)$$

To complete the picture, the velocity dependences of τ via v_i must still be inserted in Eq. (13). First the (Gaussian) distribution of fragments, characterised by σ , the inter-fragment velocity width, determines that the column density of fragments moving at a velocity v_i within the range Δv is

$$\Delta N_i = \frac{N}{\sigma} \exp\left[-\pi\left(\frac{v_i}{\sigma}\right)^2\right] \Delta v, \quad (15)$$

⁴ Here we use a somewhat unorthodox definition for the Gaussian velocity dependence. The π factors are introduced merely for simplicity and do not affect the conclusions. The relation to the width of the profile is then $\sigma_{\text{th}} = 1.06 \times \text{FWHM}$.

⁵ Define $r^2 = p^2 + z^2$, where p is the displacement variable and z lies along the line of sight. This yields $dx dy = 2\pi p dp$. And since

$$\tau(p) = \int dz n(p, z) \kappa \quad (12)$$

the area element reduces to $\pi r_{\text{cl}}^2 d\tau/\tau$.

where N is the total column density of fragments and no systemic velocity is assumed, i.e. $\langle v_i \rangle = 0$. Furthermore, to account for the velocity dependence within the fragments the Gaussian factor of Eq. (10) must still be added after τ_{cl} in Eq. (13). This then gives $\tau_{\text{eff}}(v_z, v_i)$, i.e. the effective optical depth of fragments moving at v_i , measured at v_z . For the total effective optical depth, or opacity we integrate over all v_i . Continuing from Eq. (13) this gives

$$\tau_{\text{eff}}(v_z) = \frac{N \pi r_{\text{cl}}^2}{\sigma} \int_{-\infty}^{\infty} dv_i e^{-\pi\left(\frac{v_i}{\sigma}\right)^2} \int_0^{\tau_{\text{cl}}} e^{-\pi\left(\frac{v_i - v_z}{\sigma_{\text{th}}}\right)^2} \frac{d\tau}{\tau} (1 - e^{-\tau}). \quad (16)$$

The thermal width of the fragments, σ_{th} , determines how much the second integral of Eq. (16) contributes. This in fact says that only velocities close to v_z should be considered. If now the inter-fragment width σ is at least three times σ_{th} , the variation of the first exponential around $v_i = v_z$ is negligible and can be taken outside the integral (Martin et al., 1984). Introducing this assumption and changing to opacities rather than optical depths we finally get

$$\kappa_{\text{eff}}(v) = n_{\text{cl}} \pi r_{\text{cl}}^2 \times A(\tau_{\text{cl}}) \times \frac{\sigma_{\text{th}}}{\sigma} \exp\left[-\pi\left(\frac{v_z}{\sigma}\right)^2\right]. \quad (17)$$

In which n_{cl} is the number density of fragments and $A(\tau_{\text{cl}})$ is given by

$$A(\tau_{\text{cl}}) = \int dv \int_0^{\tau_{\text{cl}} \exp(-\pi v^2)} d\tau \frac{1 - e^{-\tau}}{\tau}. \quad (18)$$

This represents the ratio of the optical thick area to the geometrical area of a fragment whose peak opacity is τ_{cl} . It also depends through τ_{cl} on the specific transition. Equation (17) can be further reduced, attributing the velocity dependence to the line profile and noting that the fragment density is given by $n_{\text{cl}} = f/V_{\text{frag}}$, in which f is the volume filling factor, which is less than unity in the case of physical clumping. A relation between the effective opacity and the standard opacity (without clumping) is then obtained:

$$\kappa_{\text{eff}}(v) = \kappa(v; \sigma) \times \frac{A(\tau_{\text{cl}})}{\tau_{\text{cl}}} \times f. \quad (19)$$

The behaviour of $A(\tau_{\text{cl}})/\tau_{\text{cl}}$ is illustrated in Fig. 1. Two regimes can be distinguished. If $\tau_{\text{cl}} \ll 1$ the A -factor grows linearly with τ . In this limit the central opacity is reduced only by $\sigma_{\text{th}}/\sigma$ because the velocity distribution is turbulent rather than thermal. This is the micro-turbulence limit. However, if the fragments become thicker and τ_{cl} approaches 1, the individual fragments become opaque and the *effective* optical depth decreases. $A(\tau_{\text{cl}})$ is no longer linear with τ_{cl} and a significant reduction in opacity can be achieved (incompressible turbulence). Moreover, if the fragments don’t fill the whole medium, $\kappa(v)$ is further reduced by the filling factor (compressible turbulence). Macro-turbulence is reached when $f < 1$ and $\tau_{\text{cl}} \gg 1$. Equation (19) is an important consequence, since it prevents the self-absorption of which non-turbulent and to a lesser extent micro-turbulent models are often plagued with, while the observations don’t show such features. Ossenkopf et al. (2001, their Fig. 1) give examples of this phenomenon.

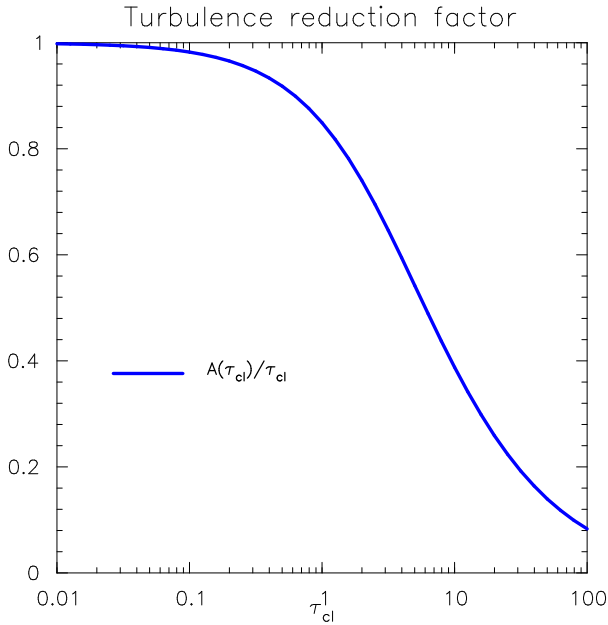


Fig. 1. The behaviour of the turbulence reduction factor, $A(\tau_{\text{cl}})/\tau_{\text{cl}}$ of Eq. (19) is shown. As the fragments grow in size and become more optically thick (incompressible-turbulence), this leads to a subsequent decrease in effective opacity.

2.3. SIMLINE input parameters

The SIMLINE code consist of two parts:

- The calculation of the level populations. Here the physical parameters (density, temperature, cloud properties) enter.
- The calculation of the emergent model profile. This requires the level populations, together with the telescope parameters and the transitions.

The input parameters for the calculation of the level populations can be specified as function of different *shells*. The code assumes spherical symmetry. The transition from one shell to another is continuous, but the radial gradients can differ. So, for every shell a scale factor (value at the inner radius) and a radial gradient are specified for the following parameters:

- inner radius r_c and outer radius R .
- H₂-density, $n(r)$
- Temperature, $T(r)$
- Abundance, $X^{\text{com}}(r) = X(r) \times f$
- Turbulent velocity, $\sigma(r)$
- Correlation length, $l_{\text{corr}} = \frac{\sigma}{\sigma_{\text{th}}} r_{\text{cl}}$
- Systematic (radial) velocity, $v(r)$

The volume factor, f enters when the clumps do not fill the whole medium. In these cases the local density (i.e. in the clumps, determining the excitation) and the average density differ. Moreover a $f \neq 1$ reduces the opacity correspondingly (Eq. 19). From a mathematical point of view this is equivalent to an artificial reduction of the abundance, since the quantity of importance in the statistical equilibrium equations, i.e. the mean intensity, is proportional to column density and thus to f .

DEFAULT MODEL PARAMETERS

Parameter	Symbol	Value
HCO ⁺ Abundance	X^{com}	1.0×10^{-9}
Inner radius	r_c	0.001 pc
Outer radius	R	0.392 pc
Hydrogen Mass	\mathcal{M}	$80 M_{\odot}$
Density exponent	p	-2.0
Correlation length	l_{corr}	0.1 pc
Turbulent velocity	v_{turb}	$0.15 \times (r/r_c)^{0.5} \text{ km s}^{-1}$
Systematic velocity	v_{sys}	0

Table 2. Parameters of the ‘Default’ model, i.e. corresponding to the two top graphs in Fig. 2. The filling factor is chosen 1 here, so $X = X^{\text{com}}$.

OBSERVATIONAL PARAMETERS

Parameter	Value	
Distance	$d = 2.7 \text{ kpc}$	
Transitions	$4 \rightarrow 3$ $3 \rightarrow 2$	
Beams (convolutions)	FWHM	line ^a
– None	1''	(black)
– JCMT	15''	(purple)
– KOSMA	100''	(light-blue)

^a Colour as in the plots of Fig. 2

Table 3. Observational Parameters of the model corresponding to Fig. 2. HCO⁺3 → 2 and HCO⁺4 → 3 are both shown, where the color indicates the beam.

So in the next sections when spoken of an abundance, a *combined abundance*, $X^{\text{com}} = X \times f$ is what is really meant.⁶

The mass of a spherical cloud, whose density distribution is governed by a power law with density exponent $-p$ and inner and outer radius r_c, R is given by

$$\mathcal{M} = \frac{4\pi\mu m_{\text{H}}}{3-p} n_c f r_c^3 \left(\left(\frac{R}{r_c} \right)^{3-p} - 1 \right), \quad (20)$$

where n_c is the H₂ density at the inner cut-off radius, μ the mean molecular weight (≈ 2.36) and m_{H} is the hydrogen mass. So given a mass and a filling factor, n_c can be calculated. Consequently we define the expression \mathcal{M}/f to be the *combined mass*.

2.4. Studying the line-profile

In this section the characteristics of the line profile with the physical conditions in the region it originates are studied. The goal is to obtain a general picture of how variations in the local conditions affect the line profile as seen by the observer. This is done by constructing synthetic profiles for which two distinct cases are presented. These two cases have exactly the same input parameters, specified in Table 2, except for the temperature structure. In the first case a model-profile without internal source is computed. Here the temperature decreases from

⁶ In Sect. 3 we will constrain f and X afterward from the results of X^{com} and the computed mass of the cloud. Another, somewhat less flexible approach, is to *assume* values for the mass and/or abundance, which directly gives the filling factor.

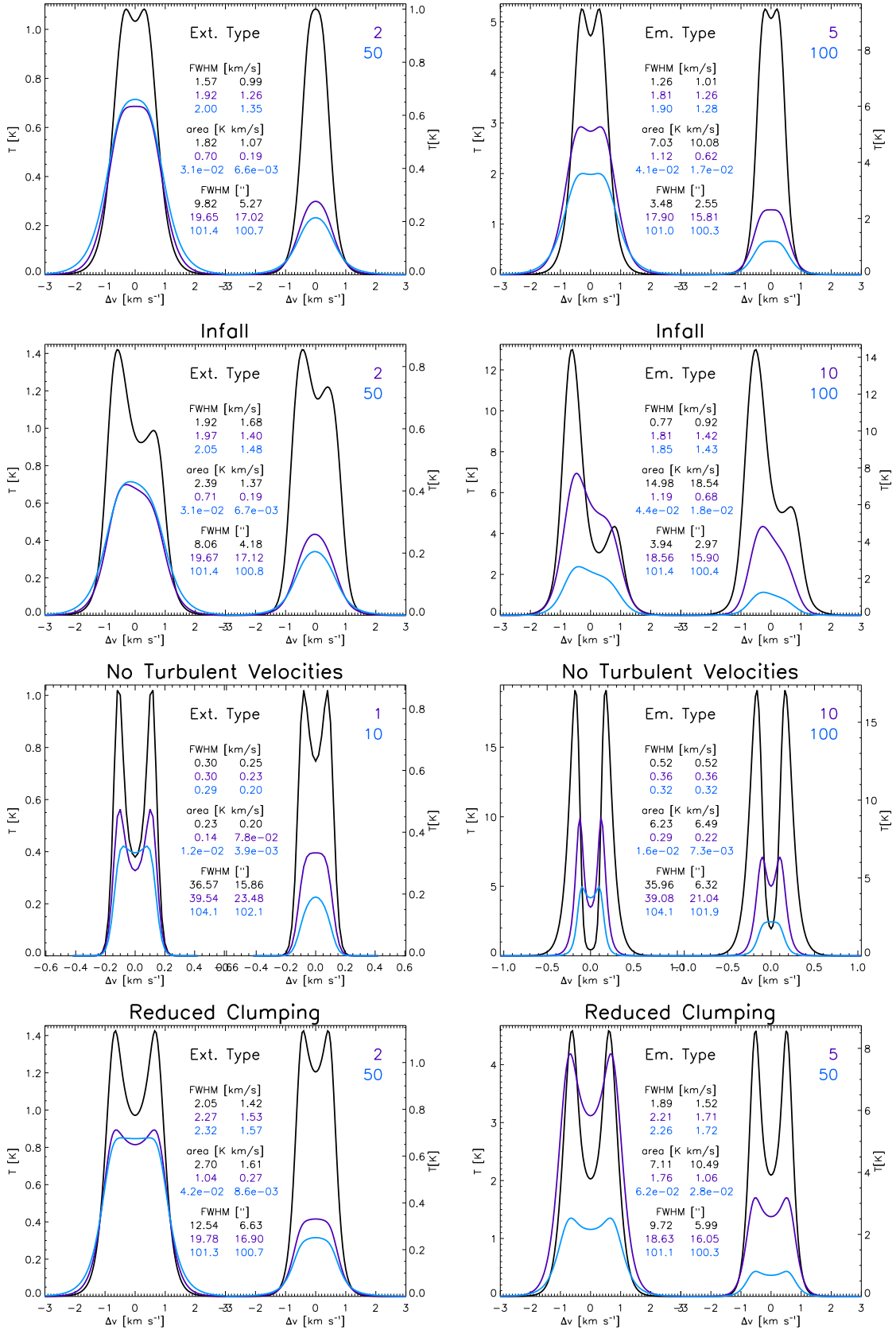


Fig. 2. Synthetic HCO⁺ line profiles. The upper two panels are the profiles of the default model, whose parameters are given in Tables 2 and 3. In each panel both transitions (left: 3 → 2; right 4 → 3) are shown. The black line is the unconvolved profile and the overplotted lines are convolved with beams of 15'' and 100'', which have been magnified by the factors given in the upper right area of the panels.

17 K at the outer boundary to 5 K at the inner cut-off radius. This is called an ‘extinction-type’ model, i.e. a model without source of which the temperature and density structure are in accordance with the result found by the continuum modelling (see Paper I). The other case, an emission type model, is represented by a two shell structure. As function of decreasing radius, the temperature profile first decreases to 10 K at 0.1 pc and then increases to 200 K at the inner cut-off radius. The remaining input parameters as given in Table 2 are the same for both cases.

For the HCO⁺ combined abundance a value of 1.0×10^{-9} was taken. In the literature one finds abundances ranging from 1.0×10^{-10} to 2.0×10^{-8} . The adopted turbulent structure is such that the resulting line widths are close to the observed 3 km s^{-1} .

It should be stressed that the adopted temperature and density structure for these model profiles are a rough estimate of the results obtained from the continuum modelling. The temperature structure, for example, is approximated by power-laws. The results here are indicative with the main purposes being to compare a ‘cold’ model with a ‘hot’-internal model, to observe the behaviour of the profiles when varying input parameters and to view the influence of the subsequent beam-convolution. Therefore profile with beams of respectively $1''$,⁷ $15''$ and $100''$ are given.

The eight panels in Fig. 2 show the results of the synthetic line-profiles. The panels on the left concern the ‘extinction type’ (cold), while the panels on the right are results from the ‘emission type’ (hot interior). In each plot both transitions are given with the absolute intensity level on the vertical axis. Moreover key parameters like the FWHM (both in velocity units at the central position and in arcseconds for $I(r, v = v_0)$) are given. Finally the beam-convolved profiles are over-plotted (in a different colour), scaled up by the factor given in the upper-right corner of each plot.

The upper panels correspond to the default parameters as specified in Table 2. In the three subsequent rows one of these parameters is altered. In the first row a systematic velocity is introduced, given by $v(r) = -2.0 \text{ km s}^{-1} (r/0.001 \text{ pc})^{-0.5}$, reflecting material that is in free-fall. The next row shows profiles without turbulence and finally in the last row the turbulent correlation length l_{cl} is decreased by a factor of 10. All lines are optically thick (typically $\tau_0 \approx 10$) and this causes self-absorption: photons emitted at the centre of the cloud are reabsorbed in the outer layers, since the excitation temperature T_X is lower here. Therefore, even though the temperature increases outwardly, like in extinction-type cases, the line can still show self absorption; T_X is no longer coupled to T (see Fig. 3).

In most cases the self-absorption disappears after the beam-convolution, though flat-top structures might leave traces, especially when convolved with a modest beam of $15''$. Exceptions are the cases without turbulent velocities (3rd row) and with reduced clumping (4th row). Thanks to the fact the lines are much more optically thick here, self-reversal traces remain. The same holds with the infall in the second row of figures. If the lines

⁷ In order to get a profile out of the level populations, a convolution had to be done. But convolving with a beam of $1''$ will not be very different from not convolving at all.

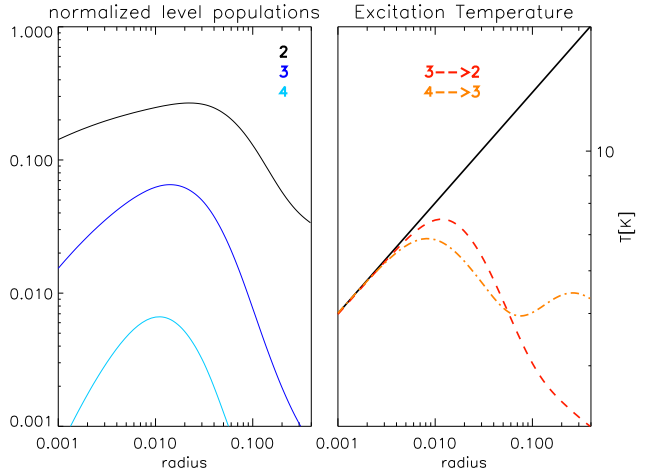


Fig. 3. normalised level populations (left) and excitation temperature (right) for the $4 \rightarrow 3$ and $3 \rightarrow 2$ transitions corresponding to the upper-left plot in Fig. 2. In the inner-most regions at densities $n \geq 10^7 \text{ cm}^{-3}$, T (black line) and T_X (red/orange lines) are well coupled. However this coupling is lost at lower densities such that the peak emissivity occurs close to the centre of the cloud.

are sufficiently optically thick, skewed traces remain even after convolving. However to detect these observationally the S/N -ratio has to be high. The discrepancy between the blue (at velocities $v < 0$) and red peak is higher if the line becomes more optically thick. The asymmetry is due to the fact that the blue peak originates in the infalling rear part of the core, where T_X increases toward the observer, while for the red part this is reversed.

The final two rows show the importance of the turbulent structure. Thermal broadening alone results in lines with widths less than 1 km s^{-1} , clearly in violation with observations. Smaller values for l_{corr} broaden the profiles; here the effective opacity reduction factor ($A(\tau_{cl})/\tau_{cl}$, Fig. 1) is closer to 1, leading to higher opacities and broadening the profile. However, from an theoretical point of view, little is known about l_{corr} and this parameter is fixed at 0.1 pc throughout the modelling in the next section.

Comparing the profiles between the left and right panels, i.e. between the ‘Emission type’ and the ‘extinction type’ three remarks can be made. Firstly, that – except in the case without turbulent velocities – the widths are all about equal. Only if turbulence velocities play no role, the FWHM is a true measure for the temperature. Secondly, self-absorption effects are stronger in cases of an embedded source. Finally, although the peak intensity is higher in the ‘emission type’ case, also the differential fall-off with increasing beam size, $dI_{peak}/d\sigma_{beam}$, is steeper. In other words observing an embedded source with a finer beam gives a higher increase in intensity than an ‘extinction type’ model would do.

In this section we have reviewed the formation of the line-profile within a turbulent-clumping setting. It was found that thermal velocities alone cannot produce line widths of over 1 km s^{-1} ; large scale turbulent motions are required. Moreover,

an inhomogeneous configuration in phase-space does not leave τ_{eff} unaffected, since it is $\langle e^{-\tau} \rangle$ which the observer is sensitive to (see Eq. 19). So with increasing clumpiness (I_{corr}), the effective opacity is reduced and the wings become optically thin such that the line narrows. Another effect on the line profile of increasing clumpiness is the diminishing of the self-absorption. Self-reversal profiles appear when a layer of sufficient thickness has a decreasing T_X in the direction toward the observer. This means either a drop of the kinetic temperature or a drop of the density below the critical level. However, self absorption – as with most of the peculiar line characteristics – are often washed out in the subsequent beam-convolution. At most top-flattened features survive, especially when the line is optically thick over a wide range in velocity or physical space. The same holds for asymmetric features, which must be sufficiently strong and skewed to ‘survive’ the beam convolution.

3. HCO⁺ modelling

3.1. Observations

In Paper I continuum observations of the W51-IRDC using JCMT’s Submillimeter Common User Bolometer Array (SCUBA) were discussed, which revealed three separate cores. One of them corresponded to the location of peak MSX-extinction⁸ and was designated extinction peak (EP), while the other two showed up even stronger at 450 μm and 850 μm and were labelled ‘P1’ and ‘P2’ respectively. Subsequent modelling showed that these ‘emission peaks’ were found to harbour embedded sources of $100 L_{\odot} \lesssim L \lesssim 1000 L_{\odot}$, while for the extinction peak results were inconclusive about the presence of a source. Also conspicuous was that P1 – the brightest peak – was slightly away from the main rim of MSX-extinction.

Moreover, observations of the W51-IRDC region have been obtained in a variety of molecular lines with both JCMT and KOSMA telescopes. With JCMT, maps have been obtained in CO $2 \rightarrow 1$, C¹⁸O $2 \rightarrow 1$ and for HCO⁺ in both J: $4 \rightarrow 3$ and $3 \rightarrow 2$ transitions. HCO⁺ maps were made on a rectangular grid spaced 5'' in Right Ascension and 10'' in declination. All spectra contain enormous low frequency standing waves and a linear baseline subtraction was done in two windows on opposite sides of the line. The HCO⁺ maps are given in Figs. 4 and 5. Moreover, a single pointing with HCO⁺ $3 \rightarrow 2$ was performed on the extinction peak.

Single pointing KOSMA observation of ‘P1’ and ‘EP’ are available in both HCO⁺ transitions. These were obtained in dual-beam switch mode, where the beam switch measures the difference between the region under consideration and a 6' away, emission free, reference. Then the off position becomes the source and the new off position is located at exactly the same 6' at the other side of the source to create the most symmetric observing situation. This process is repeated. It is interesting to remark that the KOSMA data shows the extinction peak to be more prominent in HCO⁺ $3 \rightarrow 2$ emission than P1 (Table 4), while the reverse is seen in the JCMT maps. A likely

⁸ i.e. the location where the Midcourse Space eXperiment satellite (MSX), measuring at 8.3 μm , observed the least flux.

explanation is that the large KOSMA beam probes mainly extended emission and that – since P1 seems to be slightly away from the main cloud complex (see Paper I) – this effect is more important at the extinction peak than at P1.

3.2. Model fitting

Since the SIMLINE code acts as a two-stage rocket, we can – after the calculation of the level populations – retrieve multiple model profiles as seen by different telescopes and/or in different transitions. These are then compared with the data and a χ^2 goodness-of-fit parameter is calculated. In the case of HCO⁺, after each calculation of the level populations, four profiles can then be computed: The $4 \rightarrow 3$ and $3 \rightarrow 2$ transitions with the observational parameters of both KOSMA and JCMT telescopes. However, for the modelling only the JCMT data is used, since the JCMT’s beam is most appropriate in comparison with the scales of the cores. Yet, the addition of the KOSMA data is important, since this gives important clues on the background density and temperature. (The term *background* is referred to as a medium of constant density and temperature which the cores are embedded in.) This extended material, constrained by the KOSMA data, is of importance in the modelling of the JCMT data, since as with the continuum modelling, the full JCMT beam is taken into account. The model profile is then convolved with two Gaussians, i.e. with a beam pattern approximated by

$$B(\theta) = \lambda_1 G(\theta, \sigma_1) + \lambda_2 G(\theta, \sigma_2). \quad (21)$$

In which $G(\theta, \sigma)$ are normalised Gaussian, λ_1 is the main-beam efficiency and $\lambda_2 = 1 - \lambda_1$ is the power within the error-beam, which FWHM is given by the linear extrapolation of the 850 μm error beam (see Table 5).

For the χ^2 goodness-of-fit parameter we have chosen to model the moments of the spectrum, i.e.

$$I_n = \int dv I(v) (v - v_0)^n. \quad (22)$$

So the 0th moment (I^0) is the integrated area, while the second and fourth moment are more sensitive to the width of the profile. The odd moments measure the asymmetry of the profile, but were not included in the χ^2 since these traces were not significant. We decided to stick with the 0th, 2nd and 4th moments and the strength of the self-absorption, defined as the difference between the maximum and the central (i.e. at $v = v_0$) intensities. This latter quantity is primarily added to be also sensitive to self-absorption effects.

Equation (22) is for a continuous spectrum, but in reality the spectrum has finite resolution (Δv) and this equation is then being replaced by a summation over some region ($\pm V$) of the spectrum around the peak (v_0), i.e.

$$I_n = \sum_{v_i} I(v_i) (v_i - v_0)^n \Delta v \quad |v_i - v_0| < V \quad (23)$$

Assuming a constant error, σ , for each bin of the spectrum, propagation of errors then relates the error in the moments to the rms-error in the spectrum, i.e.

$$\sigma(I_n) = \sigma \sqrt{\sum_{v_i} (v_i - v_0)^{2n} \Delta v} \quad |v_i - v_0| < V \quad (24)$$

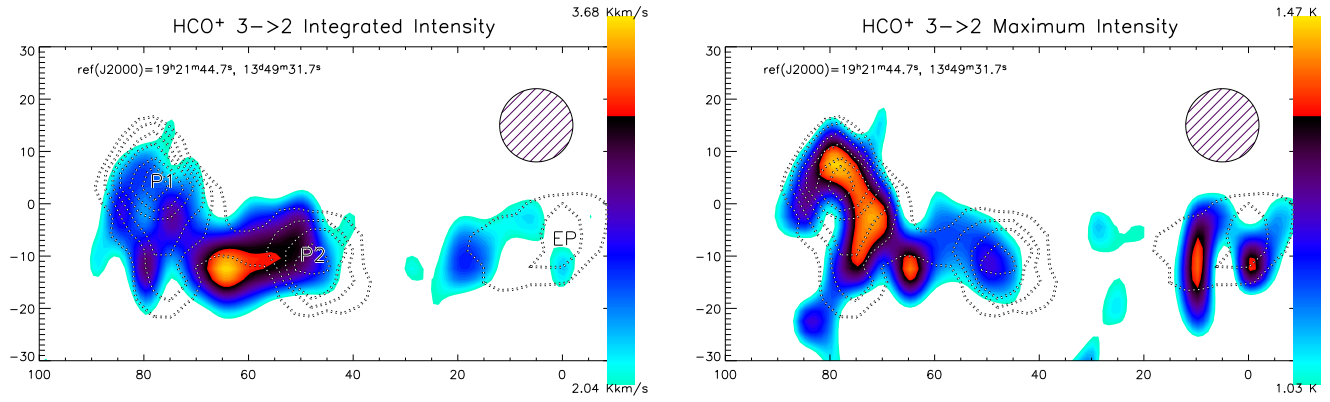


Fig. 4. Contour maps of HCO⁺ 3 → 2. The left figure shows the *integrated* HCO⁺-intensity in a window of $v = 33 \pm 3$ km s⁻¹. The value of the coloured shading is indicated by the bar at the right. The JCMT main beam is also given. The right figure shows the *maximum* intensity within the same window. The 850 μ m SCUBA dust map is overlaid with dotted contours with levels ranging from 0.25 – 0.5 Jy beam⁻¹ with increments of 0.05 Jy beam⁻¹. Clearly the dust shows a better correspondence with the peak intensity than with the integrated intensity.

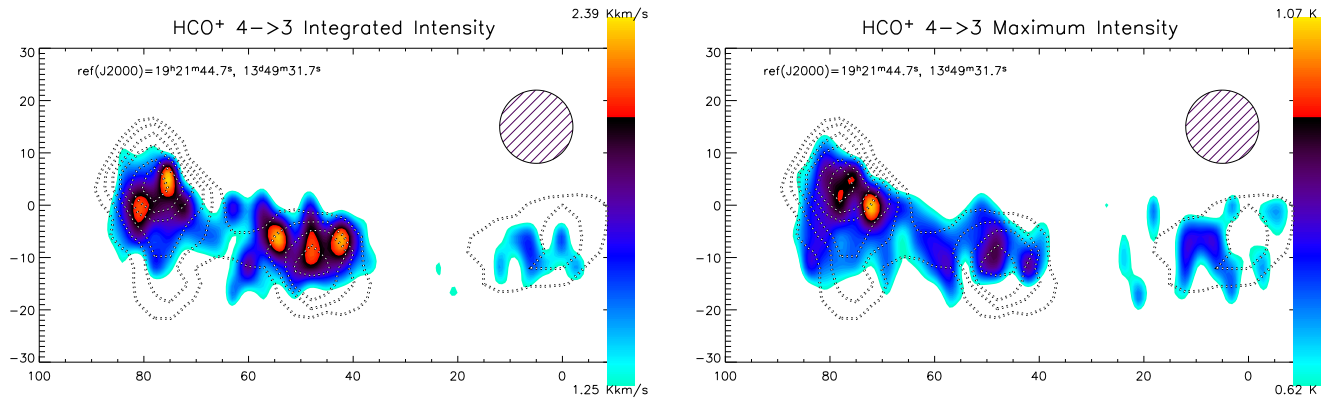


Fig. 5. Same as Fig. 4, but for HCO⁺ 4 → 3. Note also the limited intensity range the shading corresponds to, indicating that much of the space is occupied with extended emission.

The χ^2 for a specific transition j then becomes

$$\chi_j^2(\mathbf{x}) = \sum_{n=0}^2 \left(\frac{I_{2n,j} - M_{2n,j}(\mathbf{x})}{\sigma(I_{2n,j})} \right)^2 + \left(\frac{I_{\text{abs},j} - M_{\text{abs},j}(\mathbf{x})}{\sigma_j} \right)^2. \quad (25)$$

Where I_{abs} is the measured absorption dip (Table 4) and M^{abs} the modelled absorption dip, i.e. the difference between the central and the peak value of the modelled profile. M^n are the moments resulting from the model-profile. All resulting model values depend on the model parameters, \mathbf{x} (Sect. 3.3), and when modelling the JCMT data we add up the χ^2 of both transition, i.e. $\chi_{\text{tot}}^2 = \chi_{3 \rightarrow 2}^2 + \chi_{4 \rightarrow 3}^2$.

3.3. Model parameters

Since, the model is a forward model, taking the beam into account, the physical properties of the area falling within the error beam have to be considered. Figure 6 presents the geometry. The outer radius of the core, R , defines the transition from an uniform, isothermal *background* to a region ($r < R$) at which the density is represented by a power-law with exponent -2 . Although the exponent is fixed, the mass of the core can still be

BEAM PATTERN			
telescope	transition	weight factor	FWHM [arcsec]
JCMT	3 → 2	0.69	20.0
		0.31	77.0
	4 → 3	0.63	14.0
KOSMA		0.37	58.0
	3 → 2	0.68	130
	4 → 4	0.70	82

Table 5. Approximated beam pattern, used in convolving the model profiles. The distance is 2.7 kpc such that 1'' corresponds to a linear size of 0.013 pc. For KOSMA, only the main beam efficiency is given.

varied by varying R . In fact the continuum modelling (Paper I) showed that the *mass* is the most sensitive parameter, far better constrained than e.g. the density distribution. More critical was the choice for the parameters of the background (at $r > R$): $n_{\text{bg}} = 10^4$ cm⁻³, $T_{\text{bg}} = 20$ K, $r_{\text{bg}} = 0.85$ pc. The background temperature was chosen somewhat higher than the dust temperature ($T_{\text{dust}} = 17$ K), since electron-gas collisions here heat the gas (Hollenbach & Tielens, 1997). The background radius

HCO ⁺ observations								
telescope	transition	peak ^a	σ_{rms}^b [K]	FWHM [km s ⁻¹]	moments I_n^c			abs. dip ^d
					I_0 [K km s ⁻¹]	I_2 [K km ² s ⁻²]	I_4 [K km ⁴ s ⁻⁴]	I_{abs} [K]
JCMT	3 → 2	P1	0.21	2.31	2.58 ± 0.25	1.49 ± 0.42	1.95 ± 1.16	0.25
		EP	0.08	2.19	1.44 ± 0.09	0.88 ± 0.12	1.17 ± 0.26	0.05
	4 → 3	P1	0.14	2.28	2.21 ± 0.21	1.82 ± 0.43	3.63 ± 1.53	0.00
		EP	0.14	2.08	1.40 ± 0.19	0.96 ± 0.28	1.47 ± 0.65	0.15
KOSMA	3 → 2	P1	0.010	2.30	0.279 ± 0.009	0.216 ± 0.025	0.444 ± 0.106	
		EP	0.014	2.40	0.520 ± 0.013	0.423 ± 0.031	0.820 ± 0.124	
	4 → 3	P1	0.031	2.40	0.253 ± 0.025	0.206 ± 0.044	0.381 ± 0.133	
		EP	0.029	2.30	0.243 ± 0.030	0.162 ± 0.046	0.239 ± 0.119	

^a For KOSMA and the JCMT 3 → 2 transition on the extinction peak these concern single pointings.

^b Determined in windows of $15 \text{ km s}^{-1} < v < 25 \text{ km s}^{-1}$ and $41 < \text{km s}^{-1} < v < 51 \text{ km s}^{-1}$.

^c Defined in Eq. (22).

^d Strength of the self-absorption dip. The values given here are estimated by eye, the errors are the rms-noise values. See text for discussion. For the KOSMA data, no dip was observed.

Table 4. JCMT and KOSMA HCO⁺ line observations. Given as function of the specific transition and position are the rms-noise value, the width of the Gaussian fit, the 0th, 2nd and 4th moments of the profiles and finally a guess for the strength of the absorption dip.

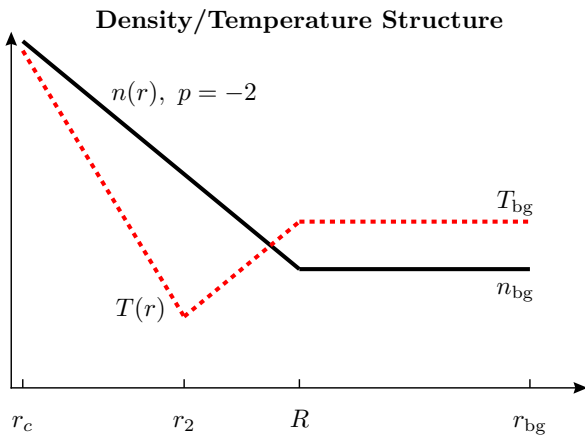


Fig. 6. Schematic picture of the density (black, solid line) and the gas temperature (red, dashed line) structure of the model description of Sect. 3.3. The situation depicted here corresponds to a model requiring three shells (i.e. P1). The parameters of the background at $r > R$ are kept constant ($T_{\text{bg}} = 20 \text{ K}$, $n_{\text{bg}} = 10^4 \text{ cm}^{-3}$), but R itself is free to vary with the density increasing with a $p = -2$ exponent toward r_c .

is sufficiently large to cope with the JCMT error beam, though a sense of arbitrariness in the choice of these values can be suspected. These have, however, been chosen such to be in agreement with the KOSMA data.

Altogether, four parameters are chosen to be optimised. They have been selected to give new information about the state of the three cores, with the fixed parameters being constrained by the continuum modelling of Paper I.

- The radius of the core, R , which, through the approach of Fig. 6, determines the combined mass (i.e. it includes the filling factor).
- The turbulent structure of the core. This gives two parameters: a scale factor (v_0 at 0.01 pc) and an exponent (v_{exp}).
- The HCO⁺ combined abundance, X^{com} .

The most important of the fixed parameters, are (apart from the already discussed background):

- The temperature structure. Apart from the background, the temperature structure as resulting from the continuum modelling is adopted, where the high densities in the inner regions ensure a strict dust-gas coupling. For P1 this means that the temperature drops to 10 K at $r = r_2 = 0.1 \text{ pc}$ and rises to values of 40 K at the inner cut-off radius (Fig. 6). For the extinction peak we adopt the sourceless model with a fairly high (though still consistent with the dust) inner temperature of 10 K, resulting in a temperature structure which can be described by one power-law only.
- The turbulence correlation length, l_{corr} . Since we know very little regarding l_{corr} this parameter was fixed at 0.1 pc, in accordance with values found by Ossenkopf et al. (2001).
- The inner (cut-off) radius, r_c is fixed at 0.01 pc. The continuum results showed that it made little sense whether the inner radius is 0.001 pc or ten times larger (in this analysis the mass of the core was held constant). For computational reasons we chose for the larger radius, since the code is much faster then.
- The systematic velocity structure, v_{sys} . Since the odd moments are all about $S/N \lesssim 1$, no systematic velocities were taken into account, so $v_{\text{sys}} = 0$ everywhere.

3.4. Results

In Table 6 results are presented for the four model parameters (Cols. 2–4): the turbulent structure (inner value and exponent), the radius and the abundance. These values correspond to the minimum of χ^2 and their fits are given in Fig. 7. The values in sub- and superscript give an indication of the degree of constraint within the specific parameter. More specifically, these values indicate the range in which χ^2 increases by at most 10%, while allowing the remaining three parameters to find their optimum values.

HCO ⁺ MODEL RESULTS							
peak	$v_{\text{turb}}(r_c)$ [km s ⁻¹]	$v_{\text{turb}}^{\text{exp}}$	R [pc]	X^{com} [10 ⁻¹⁰]	χ^2	\mathcal{M}/f [M _⊙]	$\mathcal{M}_{\text{dust}}$ [M _⊙]
(1)	(2)	(3)	(4)	(5)	(6)	(7)	(8)
P1	2.28 ^{2.45} _{2.10}	-0.33 ^{-0.27} _{-0.40}	0.70 ^{0.79} _{0.63}	0.68 ^{0.98} _{0.44}	1.04	2500 ³⁶⁰⁰ ₁₈₀₀	70 – 110
EP	2.32 ^{2.93} _{1.46}	-0.30 ^{-0.06} _{-0.46}	0.38 ^{0.46} _{0.32}	2.4 ^{4.8} _{0.96}	10.7	390 ⁷⁰⁰ ₂₃₀	110 – 150

Table 6. Results of the SIMLINE χ^2 minimization fitting-routine. Given for both peaks (Col. 1) are the values of the model parameters (Cols. 2-5) for which χ^2 (Col. 6) is minimised. Indicated in the sub- and superscript is the range for which χ^2 increases by 10%. See Fig. 7 for the fits. Col. 7 then gives the mass within R , which follows directly from the way the geometry was set up (Fig. 6). This, like X^{com} , still includes the filling factor. For comparison also the mass as found with the continuum is listed (Col. 8).

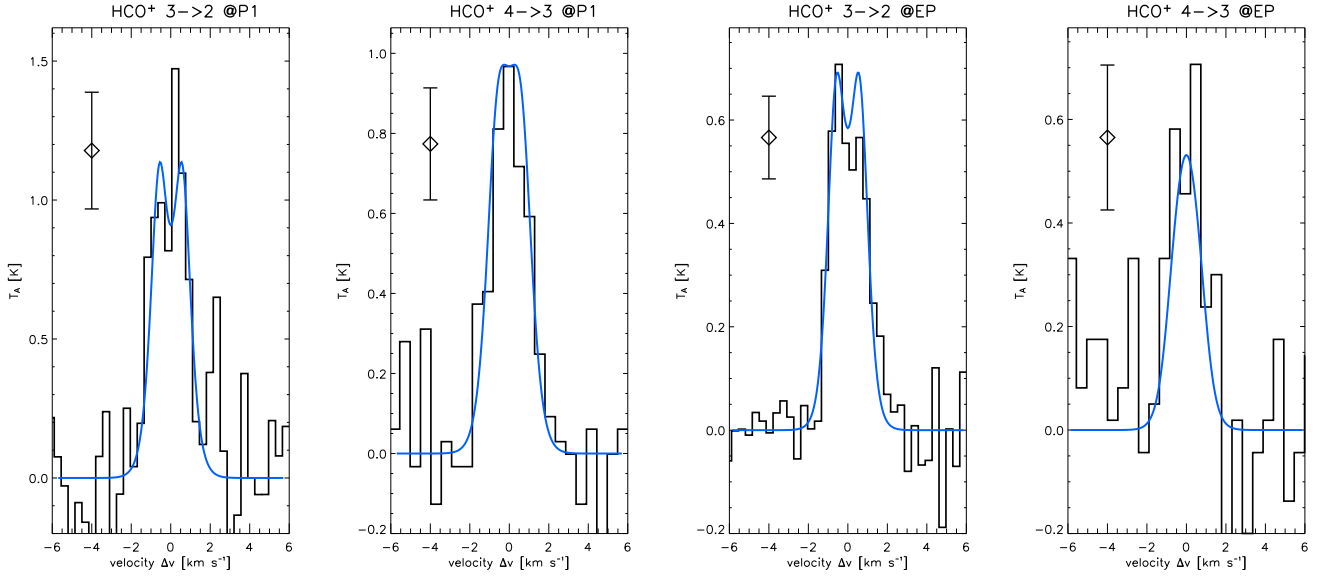


Fig. 7. Fits for the extinction peak and P1, corresponding to results given in Table 6. The rms-noise level of table 4 is also indicated.

Through the configuration of the density structure (Fig. 6), the outer radius R is directly related to the combined mass, i.e. $\mathcal{M}(<R) = 4\pi n_{\text{bg}} m_{\text{H}} \mu R^2 (R - r_c) f$. The same holds for the combined abundance, $X^{\text{com}} = Xf$, such that high combined masses (with respect to the masses found with the dust modelling) and low values for X^{com} indicate low filling-factors.

3.5. Discussion

The discussion is split in two. First the adopted fitting routine is reviewed and secondly we discuss the results.

3.5.1. Fitting Technique

As the modelling progressed, it was found that the fitting of moments, as described above, had some obvious drawbacks. It turned out that the used χ^2 -definition was especially sensitive to variations at large velocities (i.e. in the wings) and not to the characteristics of the line centre. This is understandable, since all I_n are affected by changes at high absolute v , while only I_0 is sensitive to changes around v_0 . In other words, the fitting-routine primarily fitted the wings of the line rather than the central regions. Moreover, in the case where anomalous fea-

tures were present at the higher velocities that exceeded the S/N limit (see e.g. Fig. 7, left graph near $v \approx +2.0$ km s⁻¹) this pollution led to an overall broadening of the profile, producing unreasonable fits. Therefore these features were removed in the calculation of the moments and – to be also sensitive to the line centre – the strength of the absorption dip was added as an additional fit parameters. With these modifications, we obtained reasonable results, though the approach seems somewhat artificial.

These issues are partly reflected in the large differences of the χ^2 minimum between EP and P1 (see Table 6). This in fact has several reasons. First of all the HCO⁺ 3 → 2 spectrum on EP concerns a single pointing with lower σ_{rms} (typically a factor 2-3 lower than the 3 → 2 map). Moreover it was found difficult to match the width of the 4 → 3 line. The inner temperature level T_c was adjusted to 10 K. Increasing this parameter even more would mean a departure from the two-shell structure to a situation in which (like P1) a central source is modelled. Paper I actually prefers this possibility, but the inner temperature gradients will not be that extreme as for P1. However, since the χ^2 is so sensitive to the higher moments, a major decrease in χ^2 means here that the actual fit will not *look* very different. Finally, a more fundamental problem is that – unlike the opti-

cally thin continuum – the extinction peak does not stand out in HCO⁺ with respect to its immediate surroundings (Figs. 4, 5). Clearly, this is a situation where a simple one-dimensional model is not ideal.

Altogether, the fitting routine as adopted in this paper needs modifications. The simplest case, of course, is not to fit moments at all, but just the observed spectra. Yet the idea behind fitting moments was to be insensitive to local noise-enhancements and to characterise the observed spectrum by a few meaningful parameters which can be easily fitted. Perhaps a two stage approach, in which first an analytic fit to the data is performed whereafter the moments are calculated – *cnf.* the approach of Ossenkopf et al. (2001) – is more appropriate. However in every case the moments need to be redefined. Instead of fitting the central moments (i.e. about the mean) as in Eq. (22), a better idea is to fit ‘independent’ moments in the sense that each moment expresses a unique property of the distribution. This means the fourth moment is replaced by the (excess) kurtosis, i.e.

$$\text{kurtosis} \equiv \frac{I_4}{(I_2)^2} - 3. \quad (26)$$

where the 3 takes away the contribution of the normal contribution, for which the excess kurtosis is zero. So a broader line, which increases I_2 , in principle does not have direct implications to the kurtosis. This definition also has a clear physical interpretation. A positive kurtosis indicates a peaked distribution, while a negative kurtosis means the distribution is flat.

3.5.2. Results

Notable to remark is the tight interplay between the R and X^{com} parameters. To avoid self-absorption, the fitting routine decreases the molecular abundance, yet increases the density (by increasing R) through which the inner regions remain sufficiently excited for the line to remain strong enough. Physically this corresponds to thicker clumps (higher τ_{cl}) and requires low filling factors to stay in accordance with the masses as found by the continuum and with more reasonable values for the HCO⁺ abundance. Comparing then Cols. 7 and 8 of Table 6 gives filling factors of $f = 0.036^{+0.025}_{-0.020}$ for P1 and $f = 0.33^{+0.32}_{-0.17}$ for EP.⁹ With these filling factors the abundances then become $X = (19^{+30}_{-12}) \times 10^{-10}$ for P1 and $X = (7.2^{+23}_{-5.7}) \times 10^{-10}$ for EP. These abundances are in the range of what is commonly found. For example Gredel et al. (1994) give HCO⁺ abundances of 2×10^{-8} toward the cold TMC-1 cloud, widely regarded as an upper limit, while Helmich & van Dishoeck (1997) measured warm cores within the W3 complex and found abundances in excess of 10^{-9} . Given the uncertainty range and the variation in observed HCO⁺ abundances throughout the ISM our results are reasonable. Moreover since both cores have been produced by the collapse of the same molecular cloud, it can be assumed that the abundances should be the same. Thus we can reduce

⁹ The errors in these fractions were calculated by taking the outer bounds of the (de)nominator, such to give an extreme value. For example, the upper limit on the filling factor for P1 is 110 (maximum)/ 1800 (minimum) ≈ 0.061 .

the error bars on the abundances to the overlapping region and arrive at one abundance estimate, $7.2 \times 10^{-10} < X < 31 \times 10^{-10}$. Consequently, this constraints the bounds on the filling factor, i.e. $f > 0.032$ for P1 and $f < 0.33$ for EP.

Low values for the filling factor, as found for P1, indicate the presence of high density blobs of material embedded in an overall low density environment. Low values for f are, however, not unusual. For example, Baker (1976) found filling factors of 0.01 in CO, while Park et al. (1996, and references therein) quote filling factors as ranging from 0.01 to a few tenths. Hogerheijde et al. (1995), observing the Orion bar, fitted a two component medium and found the clumps comprised 10% of the mass and 0.3% of the space. The difference between EP and P1 might simply indicate P1 to be in an advanced state of fragmentation and gives a natural explanation of why P1 and EP are different in $8.3 \mu\text{m}$ extinction as measured with the Midcourse Space eXperiment (MSX) satellite.

Since turbulence is easily dissipated in a dense medium, the question rises through what it is powered. Negative exponents as found for both peaks indicate that the ‘engine’ lies within the core, a clear hint of SF activity. For P1 this is in accordance with the results of the continuum, which showed a source of $L > 100 L_{\odot}$ had to be present. For EP the continuum results did not show the necessity of such a source, although it was not ruled out either. Implementation of a source in the model will certainly improve the fit and together with the negative exponents this gives a first hint for an additional heating source also in this core. However for EP especially the turbulent exponents give no significant constraint yet.

3.6. Conclusions, Further Work

In summary, this research was found consistent with the results of Paper I. Though many of its findings like, e.g. the temperature structure were treated here as fixed, there is one consistency check. Starting from the core masses of Paper I, abundances were derived being in good agreement with the values found commonly in the literature. Reversing the argument, this tells the mass-ranges as found in Paper I find support here. In addition the negative turbulent exponent as found for P1 indicate SF-activity and a presence of a source, and is thus in itself consistent with the assumed temperature structure. A new aspect of this paper is the conclusion that, especially for P1, the medium is clumped. Note that the clumping does not affect the results of Paper I, since the continuum is optically thin. The heavy clumping found for P1, might also give a natural explanation why it is not noticed at $8.3 \mu\text{m}$. For the EP the negative exponents and the strong $4 \rightarrow 3$ line indicate that a heating source is indeed present. Although, given the uncertainties in the parameters, the pendulum can also swing to the other side.

To investigate these conjectures, further work must concentrate in two areas. First, the reduction of the uncertainties on the (fixed) parameters by including more molecules, and secondly the modelling of more IRDC-cores. Extending the fitting routine to observations in other molecular lines is crucial in removing the more systematic uncertainties as reflected in the adopted physical structure. For example, if another pair of

transitions from a different molecule is included, the quantities to fit are doubled, while only adding one free parameter. The physical structure (i.e. the density-, temperature-, turbulent velocity-, etc.) is independent from the frequency at which the observer measures! Furthermore, besides reducing the overall uncertainty level, the modelling can be extended to other IRDC cores to investigate whether e.g. the negative turbulent velocity exponents found here are an exception or occur more frequently. Two obvious candidates are the second emission peak (P2) of the IRDC discussed here, or another IRDC, lying also in the direction of W51 for which similar data is available. At 850 μm this IRDC shows emission and could be similar to the extinction peak, though the analysis of the 450 μm data is still to be done. Finally, however, since the number of detected IRDCs exceeds the 10 000, of which many have shown to harbour dense cores, numerous sources are available.

References

- Baker, P. L. 1976, *Astron. & Astrophys.*, 50, 327
- Carey, S. J., Clark, F. O., Egan, M. P., Price, S. D., Shipman, R. F., & Kuchar, T. A. 1998, *Astrophys. J.*, 508, 721
- Carey, S. J., Feldman, P. A., Redman, R. O., Egan, M. P., MacLeod, J. M., & Price, S. D. 2000, *Astrophys. J.*, 543, L157
- Gredel, R., van Dishoeck, E. F., & Black, J. H. 1994, *Astron. & Astrophys.*, 285, 300
- Helmich, F. P. & van Dishoeck, E. F. 1997, *Astron. Astrophys. Suppl. Series*, 124, 205
- Hogerheijde, M. R., Jansen, D. J., & van Dishoeck, E. F. 1995, *Astron. & Astrophys.*, 294, 792
- Hollenbach, D. J. & Tielens, A. G. G. M. 1997, *Ann. Rev. Astron. Astrophys.*, 35, 179
- Martin, H. M., Hills, R. E., & Sanders, D. B. 1984, *MNRAS*, 208, 35
- Ossenkopf, V., Trojan, C., & Stutzki, J. 2001, *Astron. & Astrophys.*, 378, 608
- Park, Y.-S., Hong, S. S., & Minh, Y. C. 1996, *Astron. & Astrophys.*, 312, 981
- Tielens, A. G. G. M. 2003, *Lecture Notes ISM*, 1, 1
- van der Tak, F. F. S., van Dishoeck, E. F., Evans, N. J., Bakker, E. J., & Blake, G. A. 1999, *Astrophys. J.*, 522, 991

IV. Concluding Remarks

Reflecting this project – which lasted about one year, from August 2003 till August 2004 – the feeling must be a satisfactory one. Not all of the original goals were achieved – the original plan included e.g. the running of a chemistry model – but this is characteristic for planning such long time schemes. Nevertheless, the knowledge about the W51-IRDC and its cores increased dramatically and we have been able to answer key questions, with the quality of the observations often being the limiting factor.

The physical structure of the cores has been established as good as was possible. All cores have rather steep power laws, with density exponents of $p \approx 2$ or higher. Radii were more tedious to constrain, since this depended very much on the arbitrary choice where it was decided the data ‘belonged’ to the core no more. In fact this ‘cut-off’ radius determined the core’s size. This in turn reflected the density distribution; small cut-off radii resulted in a wide range of density-exponents that were still acceptable.

We were successful though in constraining the two main model parameters: the mass of the core and the luminosity of its inner source. Masses are all about $M = 100 M_{\odot}$ (somewhat higher for the Extinction peak) but the astonishing thing is that the 1σ error limits are all constrained rather tight (within $\sim 20\%$). For the Emission peak (P1), this posed a problem, since it is hard to explain why P1 with such a mass is so unnoticed in MSX. An idea was that additional $8 \mu\text{m}$ emission due to a hot source compensated the absorption. But this required very luminous sources indeed, which would then have been detected by IRAS and the idea was ruled out. In fact the IRAS non-detection combined with a $100 M_{\odot}$ massive core set an upper limit to the luminosity of the central source of $L \lesssim 1000 L_{\odot}$. So OB stars were ruled out, and the best fit for the emission peaks indicated luminosities of about $300 L_{\odot}$ are present. Though, with the error bars varying by a factor of three, these are less well constrained than the masses.

However, for the emission peaks, zero-luminosity sources were ruled out and this did answer the key question: A source had to be present. Given these luminosities it is hard to think of anything but stellar. However, in the strict sense we have merely shown a source has to be there, not what its nature is; stars, especially of high mass, do not form alone. However, it is often the most massive star that overshines its neighbours and the most simple explanation is that the bulk of the luminosity is from an intermediate mass, $\approx 3 M_{\odot}$, star. Finally, for the Extinction Peak things are not this

clear. Here the models tend to a modest source of several tens of solar luminosities, but a zero-luminosity model would still yield a fit only $\simeq 1\sigma$ worse. In the subsequent line modelling we choose for the latter; giving a qualitative distinction between the Emission peaks (P1, P2, with a hot inner region) and the Extinction peak.

The line modelling¹ gave new results about the nature of the cores. The modelled abundances were in agreement with values often cited in the literature (which show, however, a large spread) and the modelling yielded new results about the velocity structure and the mass distribution. Although, no line asymmetries were observed, the decreasing turbulent velocity with increasing radius indicates the turbulence is powered from within, suggesting SF. The fact that this also was the case for the Extinction peak might indicate something is present there indeed and that perhaps when this is incorporated in the temperature structure, the quality of the fit will improve. For P1 the main finding was its filling factor. Values of f in the order of 0.01 are not unusual though and this gives also a natural explanation why P1 is unnoticed in MSX.

There are two obvious way to extend this project. The first route is toward other (IRDC) cores, and the second is a further sophistication and extension of the current models. This latter route might include more molecular lines, through which the results will be far better constrained, or e.g. the modelling of high resolution (interferometric?) continuum observations. Moreover, from the theoretical point of view, one could think of looking into the *hydrodynamics* of the cores. The equation of state, $P \propto \rho^\gamma$, follows readily from the temperature and density distribution ($\gamma - 1 = \frac{d \log T}{d \log n}$) and it is certainly worth further exploring this aspect.

However, before modelling other IRDC/cores, a sophistication of this project might be worthwhile. Apart from the computational point of view (much of the code must be cleaned up and be better structured and also its speed can probably be improved), the fitting routine used in the line modelling should, as discussed in Paper II, be modified. Nevertheless it is the experience which perhaps is the most valuable gain. The reader should be aware that the compact writing up of the results is preceded by a rather time consuming period of careful thinking and passionate discussions. For example, considering the (continuum) data, it took some time in finding a scientific appropriate way to deal with the data and to assign errors to it. Also, the quest to set up the programs in such a way in order for the routine to automatically iterate toward the χ^2 -minimum took its time. But these ‘hobbles’ were taken and the state now reached is that this project can be ‘easily’ extended.² In the sense that when challenges are succeeded, new ones appear, this project is unfinished.

¹For reasons of time, only P1 and the Extinction peak were modelled. Contrary to what might be expected from the continuum, P2 is, however, rather different in HCO⁺ than P1: Its width is much broader and it also shows some self absorption.

²In fact I dare to claim that, given the current experience, when redone, this project can be shortened to one month instead of one year.

List of Acronyms

2MASS	Two Micron All Sky Survey
CMB	Cosmic Microwave Background
FIR	Far InfraRed
GMC	Giant Molecular Cloud
IMF	Initial Mass Function
IRDC	InfraRed Dark Cloud
IRAS	InfraRed Astronomical Satellite
ISOCAM	Infrared Space Observatory Camera
ISRF	InterStellar RadiationField
JCMT	James Clerk Maxwell Telescope
KOSMA	Kölnner Observatorium für Submillimeter Astronomie
MIR	Mid InfraRed
MSX	Midcourse Space eXperiment
NIR	Near InfraRed
PDR	Photon Dominated Regions
SCUBA	Submillimeter Common User Bolometer Array
SED	Spectral Energy Distribution
SF	Starformation
UV	Ultra Violet
YSO	Young Stellar Object

Acknowledgments

Finally, I want to conclude with some words of thanks.

First of all these go to my supervisors, *Frank*, *Russ* and *Volker*. The word ‘supervisor’ is, I think, actually misleading. In practise I rather felt to be a full member of a team. And what a formidable team it was! Its diversity certainly helped me to get the best out of the project. I had a great time, and many good memories to look back to.

Also, I want to thank my colleague students at the institute. Without e.g. the regular coffee breaks life is much harder. Thanks to *Christiaan* for his help on his self-created user interface, I used in the initial stage of the project. Thanks to *Erwin* for his help on IDL and to *Edo* for the KPLOR tips. Finally, I have good memories to the 2:30 pm (or so) tea break my roommates so persistently observed.

Finally, I must mention the people at Cologne, with whom I spent two weeks on Gornegrat in december 2003. I certainly learned much and had a great time there at 10 000 feet, together with *Martin*, *Carsten* and *Holger*.